UNIVERSITÀ DEGLI STUDI DI BERGAMO

EFFECT OF WETTABILITY ON PHASE CHANGE PHENOMENA

Fabio Villa
Doctoral Thesis

UNIVERSITÀ DEGLI STUDI DI BERGAMO
Dipartimento di Ingegneria

DOTTORATO DI RICERCA
IN
TECNOLOGIE PER L'ENERGIA E L'AMBIENTE

XXVIII ciclo

anno 2017

Effect of Wettability on Phase Change Phenomena

Doctoral thesis:
Fabio Villa

Supervisor:
Prof. Marco Marengo

Abstract

Boiling heat transfer is an effective mechanism that can remove a large amount of thermal energy from a surface owing to the high heat transfer coefficients (10^3 –10^5 W/m^{2}K), thus maintaining relatively low surface temperature. The boiling heat transfer phenomenon has been applied to several engineering and industrial fields requiring the removal of high heat flux, such as power plants, electronic chip cooling, and marine ship power generation. The improving of phase change heat transfer has been at the forefront of engineering research for decades. In this work the effect of surface wettability in pool boiling heat transfer is studied. The pool boiling phenomena is characterized by three important parameters: onset boiling temperature (T_{ONB}), the heat transfer coefficient (HTC) and the critical heat flux (CHT). All these parameters are influenced by the wettability characteristics of the boiling surface (wettability of a surface can be can be characterized by equilibrium contact angle). The experiment presents in this work reveal a reduction of T_{ONB} (down to 103°C for a super-hydrophobic test surface) the equilibrium contact angle increases, that is desirable for enhancement of pool boiling heat transfer. However on surface with a extremely high contact angle (called super-hydrophobic surfaces, SHS) the early formation of a vapor film, hinders to use super-hydrophobic surface in pool boiling condition.

Therefore an heterogeneous "biphilic" surface with two degree of wettability (SHS points dispersed on the hydrophilic surface) is proposed in this work. A biphilic surface allows to reduce the T_{ONB} (about 104°C) compared with pure hydrophilic surface (117°C for smooth stainless steel test surface) and increases the CHT by inhibition of the vapour formation at once. A SH polymeric coating, that is a patent pending, is tabled as final results of this work. A basic surface treated by SH polymeric coating enhances the pool boiling parameter (T_{ONB}, HTC and CHT). The coating shows even an excellent durability of its wettability properties also after considerable number of thermal cycle test (up to 506). The work include also some numerical simulation of pool boiling phenomena to clarify the physical behavior. Numerical simulation reveals that a dynamic contact angle treatment gives good results regarding both the bubble detachment characteristics as well as the apparent contact angle revolution with time, in comparison to the corresponding experimental data.

 Key words: Pool boiling, wettability, bubble characteristics, Volume – Of-Fluid method, contact angle, superhydrophobicity.

Contents

Contents

List of Figures

List of Tables

Chapter 1

1 Motivation of the study

1.1 Boiling application

Boiling heat transfer is defined as a mode of heat transfer that occurs with a change in phase from liquid to vapor. There are two basic types of boiling: pool boiling and flow boiling. Pool boiling occurs on a heating surface submerged in a pool of initially quiescent liquid. Flow boiling occurs in a flowing stream of fluid, where the heating surface may be the channel wall confining the flow. The heat transfer augmentation caused by boiling has been of great concern to researchers due to its potential to improve the cooling systems of many engineering applications such as electronics, nuclear reactors and high power generation (Figure 1).
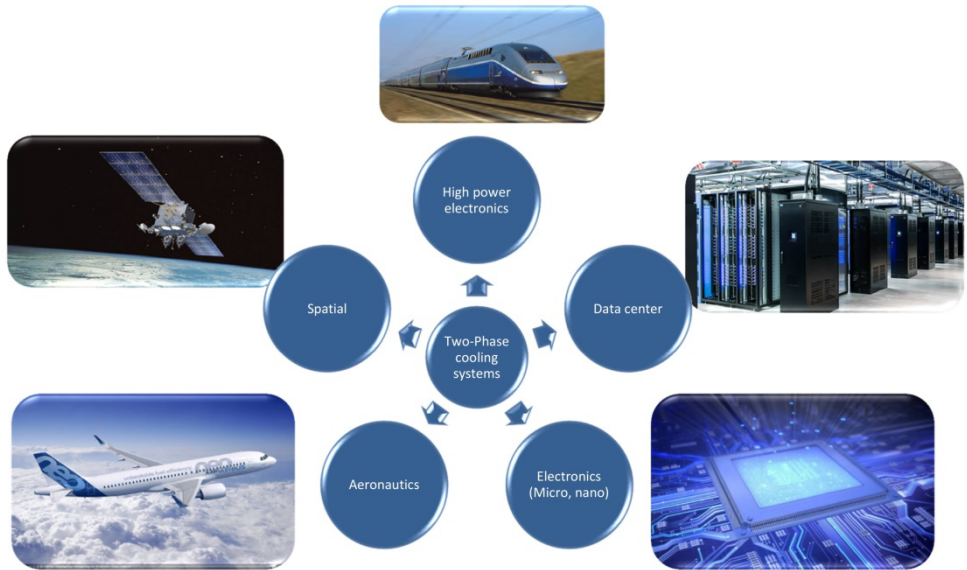
Figure 1: Two-phase cooling system

The high heat transfer coefficient that boiling heat transfer can reach (up to 10 time higher than force convective heat transfer [1]) makes it attractive especially in the thermal cooling of miniaturized systems (microelectronic and MEMS devise). The miniaturization usually facilitates thermal exchange: the characteristic thermal diffusion times are shorter in miniaturized systems and the heat flux exchanges at a fixed temperature difference are larger. On the other hand, it is difficult to impose a temperature difference in the middle of a small microsystem [2].
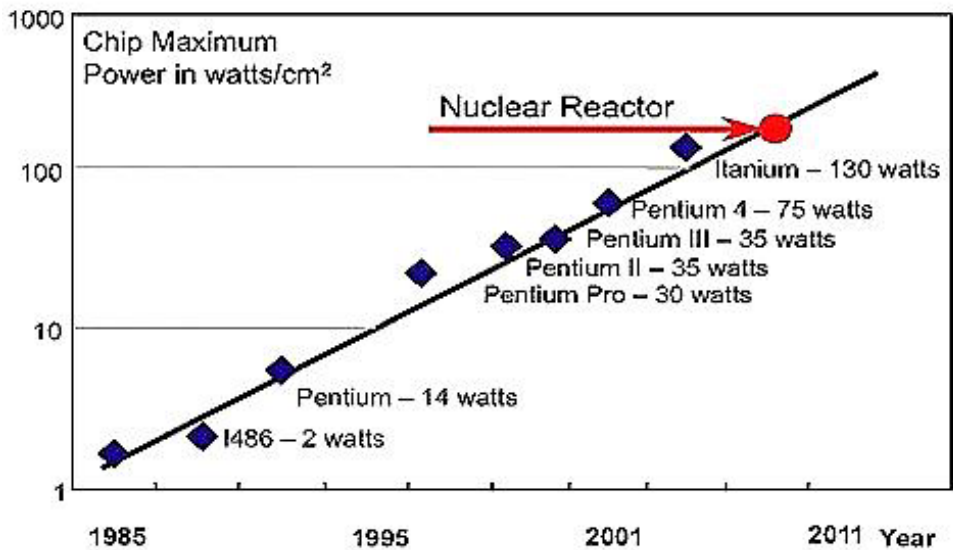
Figure 2:Temporal evolution of the chip maximum power (W/cm2) [3].

In this case the liquid–vapor phase transition can be advantageous in conventional exchangers for two reasons: the phase transition absorbs energy at a fixed temperature and the specific energy absorption (due to phase change) is definitely higher than single phase change. Since the invention of the integrated circuit, the increasing in the density of transistors is accompanied by an increase in the number of commutations operated by the chip, and the amount of maximum power to dissipate. Figure 2 shows the evolution by years of some chips maximum power.

3

Currently, radiators for microchip or MEMS devises are fabricated using an excellent heat conductor (copper), ventilated, or traversed by minicanals covered by liquid coolant. A more efficient technique uses phase change transition (pool boiling) to remove heat directly from the surface to effectively manage the thermal heat transfer needs [4]. An enhancement of pool boiling heat transfer condition can be achieved by providing additional bubble nucleation sites on the surface and/or increasing the heat transfer surface area. One of the most promise configuration used a two-phase microchannel heat sinks. Thome [5] present a summary of recent research on boiling recent research on boiling in microchannels. These researches have concluded that nucleate pool boiling controls evaporation in microchannels. In a more recent review, Baldassari et al.[6] includes the state of the art of research on internal forced convection boiling in microchannels and in microgravity conditions. A channel is usually defined as "microchannel" if the hydraulic diameter of the channels is smaller than the capillary length of the working liquid. However identifying the threshold beyond which a two-phase flow may be considered "micro" is an open issue and different classification based on the hydraulic diameter of the channels [7] or adimensional parameter [8] can be found in the literature. Microchannel heat sinks are used in high-heat flux systems, e.g., microelectronic, optical and microfluidic devices, high-performance supercomputers, electric vehicles, advanced military avionics, power and laser devices,

very-high temperature gas-cooled reactors, radiator panels of spacecraft, thermal control of satellites, etc. In pharmaceutical and chemical industries, by integrating heat exchangers, mixers, and reactors as a block of micro components, it is possible to achieve a significant decrease in the system size. Heat exchangers based on microscale channels are also used in automotive fuel cells where the heat dissipation system should be compact and contain a minimum number of components.

Chapter 2

2 State of the art: Pool Boiling enhancement

2.1 Introduction on Pool boiling

Boiling is a common energy heat transfer technique. It occurs when a liquid is exposed to a surface which is maintained above saturation temperature. Boiling can be homogeneous or heterogeneous (Figure 3). In the homogenous boiling the temperature of the liquid rises far above the saturation temperature, the vapor is formed, "nucleate", as bubbles within the bulk of the liquid causing "volumetric" or "bulk" pool boiling. Conversely in the heterogeneous boiling the nucleation appears in a liquid close to a solid surface. In the heterogeneous boiling the wall temperature (T_{wall}) of the liquid does need to be higher than saturation temperature of the liquid (T_{sat}).. If the wall temperature is sufficiently high compare a

thin layer of vapor is formed. This condition, characterize by a vapor film formation on the heated surface, is called film boiling.
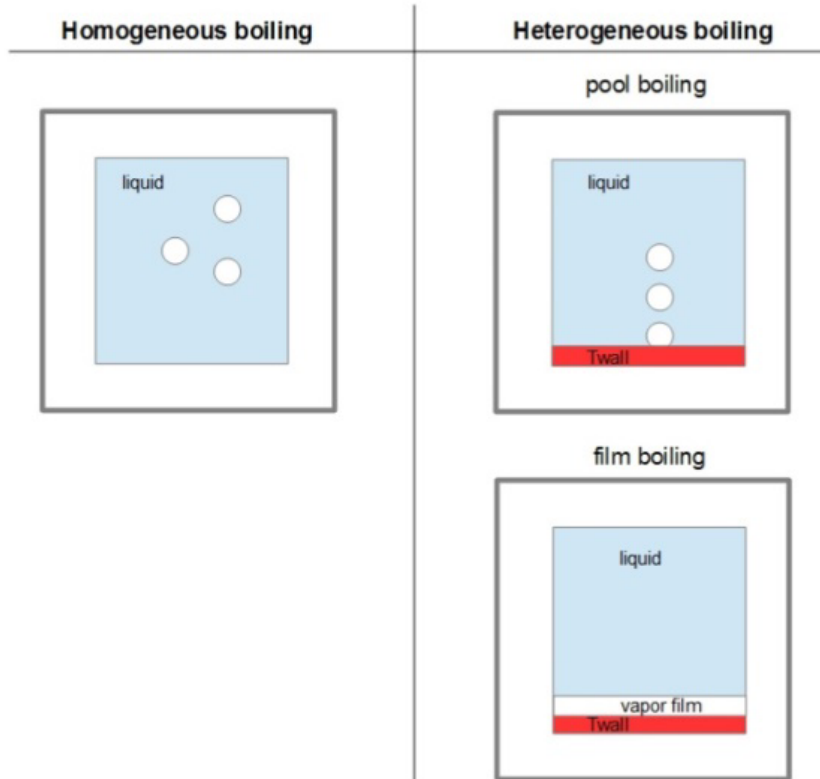
Figure 3: boiling forms. homogeneous and heterogeneous boiling. The heterogeneous boiling can be divided into pool and film boiling.

➢ The extensive study on the effect of the very large difference ($\Delta T_{sh} = T_{wall} - T_{sat}$) between temperature of the heating surface (T_w) and the saturate liquid (T_{sat}), ΔT_{sh}, was firstly done by Nukiyama [9]. However, it was the experiment by Farber and Scorah [10] that gave the complete picture of the heat transfer rate in the pool boiling process as a function of ΔT_{sh}. The various regimes of boiling in a typical case of pool boiling in water at atmospheric pressure are shown in Figure 4. It is the conventional log-log representation of heat flux versus wall superheat [9]. Different range can be identified while ΔTsh is increased:

➢ **Stage I:** the water is heated by natural convection. With the mechanism of single-phase natural convection, the heat transfer rate q'' is proportional to $(\Delta T_{sh})^{5/4}$ [11].

➢ **Stage II:** the liquid near the wall is superheated and tends to evaporate, forming bubbles wherever there are nucleation sites such as tiny pits or scratches on the surface. The wall temperature to have the nucleation of the first bubble is called *onset nucleation boiling* (ONB) ($T_{wall} = T_{ONB}$). The mechanism in this range is called *nucleate boiling* and is characterized by a very high heat transfer rate for only a small temperature difference. There are two sub-regimes in nucleate boiling: local boiling and bulk boiling. Local boiling is nucleate boiling in a subcooled liquid, where the

bubbles formed at the heating surface tend to condense locally. Bulk boiling is nucleate boiling in a saturated liquid; in this case, the bubbles do not collapse. The heat flux, q'', for pool boiling regime varies as $(\Delta T_{sh})^n$, where n generally ranges from 2 to 5.

➢ **Stage III:** the increasing of q'' with ΔTsh is limited by a condition called *critical heat flux* (CHF), which is also called a boiling crisis or departure from nucleate boiling (DNB). CHF is the condition where the vapor generated by nucleate boiling becomes so large that it prevents the liquid from reaching and rewetting the surface.

➢ **Stage VI:** immediately after the critical heat flux, boiling becomes unstable and the mechanism is then called *partial film boiling* or transition boiling. The surface is alternately covered with a vapor blanket and a liquid layer, resulting in unstable condition, that easily move to a film boiling regime. .

➢ **Stages V-VI:** a stable vapor film is formed on the heating surface and the heat transfer rate reaches a minimum. This is called *stable film boiling*. By further increasing the wall temperature, the heat transfer rate also is increased by thermal radiation. However, the high temperature reached in this stages would damage the wall. Hence, for practical purposes, the temperature is limited by the material properties.
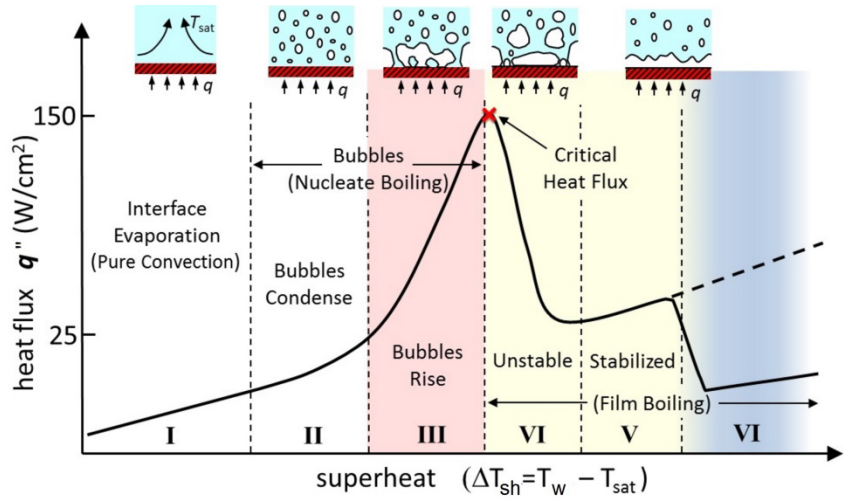
Figure 4: Pool boiling of water on a horizontal plate at 1
atm.[1]

This work is focused on pool boiling phenomena (stage II-III), looking in
detail the generation of a single bubble (Figure 5). When the wall
temperature reaches the condition Twall=TONB, a vapor bubble
nucleates on the heater surface.. The bubbles grow rapidly in the
superheated liquid layer next to the surface until they depart and move to
the bulk liquid. While they rise as the result of buoyancy, they either
collapse or continue their growth, depending on whether the liquid is
locally subcooled or superheated. The life of a single bubble may be

summarized as occurring in the following phases: nucleation, initial growth, intermediate growth, detachment and waiting time.

nucleation	Initial growth	intermediate growth	detachment	waiting time
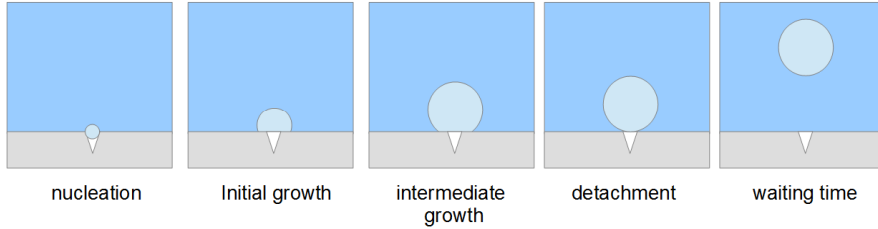
Figure 5: phases of the pool boiling phenomena

The evolution of the bubbles determines the efficiency of the heat exchange during pool boiling. It is influenced by many parameters like temperature of the surface, pressure of the liquid (Farber and Scorah [10] suggested that increasing the pressure, for the same temperature difference, would result in the decreasing of the size of the bubbles) liquid properties and surface characteristics. The next paragraph presents the main parameters to take into account for the enhancement of pool boiling heat transfer. On the next chapter the influence of surface characteristics are exposed in detail, describing the most prominent technique to improve the heat exchange during pool boiling modifying the surface topology and the wetting properties of the surface.

2.2 Pool Boiling parameters

Three main parameters must be taken into account in the enhancement of the pool boiling heat transfer:

 ➢ Onset nucleation temperature T_{ONB}

 ➢ Heat transfer coefficient HTC

 ➢ Critical heat flux CHT

The values of these parameters are strongly linked with the evolution of the bubbles (Figure 5).

Onset nucleation temperature

The early work of Bankoff [12] has shown that superheats associated with heterogeneous nucleation are much smaller than those associated with homogeneous nucleation. The reason is that a lower inception superheat can be easily rationalized if one considers that the cavities generally trap air or other non-condensable vapor. These cavities have radii generally much larger than the critical radius of the cluster of activated molecules. The volume of air trapped in a cavity depends on the magnitude of surface tension, the shape of the cavity, and the experimental conditions(such as system pressure, liquid temperature and temperature of

the heated surface). The wall temperature at which nucleate boiling begins strongly depends on the availability of cavities with trapped gas (unflooded cavities). Thus, the cavities become fewer and fewer and their size decreases, the nucleation temperatures will approach homogeneous nucleation temperature.

Consider the simplest case of a spherical vapor bubble of pressure (P_g) in a saturate liquid (T_{sat}, P_{sat}). Mechanical equilibrium [13] requires that:

$$P_g - P_{sat} = \frac{2\sigma}{r} \hspace{3cm} (2.1)$$

where σ is the interfacial surface tension and r is the bubble radius of curvature. If the liquid is superheated (a liquid is heated to a temperature higher than its boiling point), vapor bubbles form spontaneously. This liquid superheat ΔT_{sh} corresponds to a critical value of bubble radius R_{cr} [14]:

$$R_{cr} = \frac{2\sigma_{lg} T_{sat}(v_g - v_l)}{h_{lg}\Delta T_{sh}} \hspace{3cm} (2.2)$$

This formula says that a bubble of the radius $R<R_{cr}$ is not stable, so that the vapor condenses and disappears. For a bubble of radius $R=R_{cr}$ to be at equilibrium state. Finally if $R>R_{cr}$ the bubble will grow from the heat transferred by thermal diffusion from the liquid to the bubble's surface. This equation is valid for a uniformly heated liquid and semi-spherical bubble. Furthermore, experimental observations [15] have indicated that

growing bubbles are not hemispherical, but elongated. An improvement of the correlation is made by Wang and Dhir [16]. They examined the conditions that are sufficient for the occurrence of vapor/gas entrapment in a cavity, based on the minimization of the Helmholtz free energy of a system containing a gas–liquid interphase. Their criterion for the entrapment of vapor/gas in a cavity (which is equivalent to the occurrence of a minimum of excess Helmholtz free energy on or in the cavity) is:

$$\theta > \psi_{min} \qquad\qquad (2.3)$$

Where ψ_{min} is the minimum cavity-side angle (Figure 6). For a spherical cavity, the corresponding saturation temperature inside the bubble can be approximately found from the Clausius-Clapeyron equation, and introducing a constant to take into account the contact angle (wettability effect) of the surface (θ). Wang and Dhir [16] derived the following inception criterion:

$$T_w - T_{sat} = \frac{2\sigma T_{sat}}{\rho_g h_{lg} R_C} K \qquad\qquad (2.4)$$

Where

$$K = \begin{cases} 1 & for\ \theta \le \dfrac{\pi}{2} \\ \sin\theta & for\ \theta > \dfrac{\pi}{2} \end{cases}$$
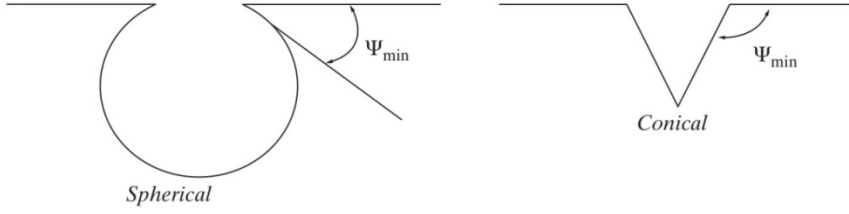
Figure 6: minimum cavity-side angle for spherical and conical cavity.

Then assuming a linear temperature drop in the thermal boundary layer, one can express the temperature profile in the boundary layer as:

$$T(y) - T_l = (T_w - T_l)\left(1 - \frac{y}{\delta_t}\right) \tag{2.5}$$

For a particular wall superheat, it is possible to apply Hsu's criteria[17], that is shown in Figure 7. The interception between inception criterion (Clausius-Clapeyron equation) and the equation of the thermal boundary layer gives the range of possible nucleating cavities ($r_{c,min} < r_{c,o} < r_{c,max}$) .

For a given wall superheat, the two radius are:

$$\{r_{c,min}, r_{c,max}\} = \frac{\delta_t C_2}{2C_1} \frac{\Delta T_w}{\Delta T_w + \Delta T_{sub}} \times \left[1 \pm \sqrt{1 - \frac{8C_1 \sigma T_{sat}(p_l)(\Delta T_w + \Delta T_{sub})}{\rho_v h_{fg} \delta_t (\Delta T_w)^2}}\right]$$

$$\tag{2.6}$$

Where $C_1 = 1 + cos\theta$; $C_2 = sin\theta$; $\Delta T_w = (T_w - T_{sat})$; $\Delta T_{sub} = (T_w - T_l)$
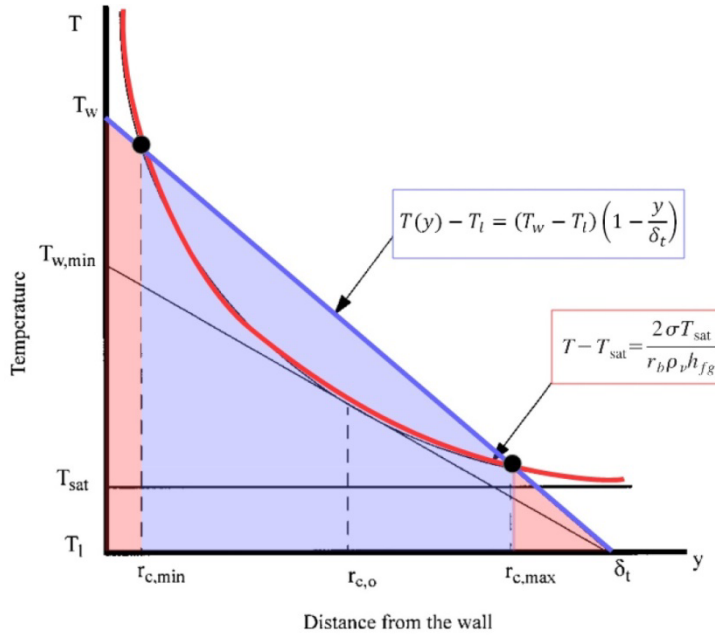
Figure 7: Inception criteria [16]

Heat transfer coefficient

For a nucleate boiling on an upward-facing horizontal surface in the isolated bubble region, heat transfer mechanisms include [18]:

> ➤ **Transient heat conduction** from the heating surface to the adjacent liquid.

➢ **Natural convection** on inactive areas of the heating surface.

➢ **Evaporation from the micro layer** underneath the vapor bubble.

$$q'' = \underbrace{\frac{C_1^2}{2}\sqrt{\pi(k\rho c_p)_\ell f_b} D_b^2 N_a'' \Delta T}_{\text{transient conduction}} + \underbrace{\left(1 - \frac{C_1^2}{2} N_a \pi D_b^2\right)\bar{h}_{nc}\Delta T}_{\text{natural convection}} + \underbrace{N_a''\frac{\pi}{4}D_b^2 \bar{h}_{evp}\Delta T}_{\substack{\text{micro layer} \\ \text{evaporation}}}$$

Figure 8: expression of the heat flux during partial nucleate boiling [18]. $C1$ is the proportionality constant for bubble area influence, D_b the bubble diameter at departure, the bubble release frequency f_b, the number density of the nucleate site N_a'', and $\bar{h}_{nc}, \bar{h}_{eva}$ average heat transfer coefficient of natural convection and evaporation.

Equation in Figure 8 shows that the heat transfer due to phase change (micro layer evaporation) increases in these cases:

➢ the bubble frequency increases.

➢ the nucleation site increase.

➢ The diameter of the bubble increases.

The problem with equation in Figure 8 is that it is impossible to get closer than one empirical constant since the nucleation site distribution is

17

unknown *a priori*. A more useful relation can be obtain using the Buckingham pi-theorem. The pool boiling heat transfer could depend on the difference between the surface and saturation temperature ($\Delta T_w = T_w - T_{sat}$) , the body force arising from the liquid-vapor density difference ($g(\rho_l - \rho_v)$) , the latent heat h_{vl}, the surface tension σ, a characteristic length L and the thermophysical properties of the liquid or vapor (ρ, c_p, k, μ).

$$h_{boiling} = h[\Delta T_w, g(\rho_l - \rho_v), h_{vl}, \rho, c_p, k, \mu] \qquad (2.7)$$

Using dimensionless group this relation can be written as:

$$Nu_L = f[Gr, Ja, Pr, Bo] \qquad (2.8)$$

➢ $Nu = \dfrac{hL}{k}$: *Nusselt number*, ratio of convective to conductive heat transfer across the boundary.

➢ $Gr = \dfrac{g\rho(\rho_l - \rho_v)L^3}{\mu^2}$: *Grashof number*, the ratio of the buoyancy to viscous force acting on a fluid.

➢ $Ja = \dfrac{Cp(T_w - T_{sat})}{h_{vl}}$: *Jakob number*, ratio between sensible to latent energy absorbed during liquid-vapor phase change.

➢ $Pr = \dfrac{\mu Cp}{k}$: *Prandlt number*, ratio of momentum diffusivity to thermal diffusivity.

18

➤ $Bo = \frac{g(\rho_l - \rho_v)L^2}{\sigma}$: *Bond number*, ration of body force to surface tension.

One of the most famous empirical correlation is obtained by Rohsenow [19]:

$$q'' = \frac{\mu h_{lv}}{L}[Bo]^{1/2}\left[\frac{Ja}{C_{s,l}Pr^n}\right]^3 \qquad\qquad (2.9)$$

Critical heat flux

In nucleate boiling, heat flux increases and reaches a maximum value with increasing surface temperature. The maximum heat flux that can be obtained by nucleate boiling is referred to as critical heat flux CHF (see Figure 4). Immediately after the critical heat flux has been reached, boiling becomes unstable and the mechanism is then called partial film boiling or transition boiling. In the case of controlled heat flux, a slight increase of heat flux beyond the CHF can cause the surface temperature to rise to a value exceeding the surface material's maximum allowable temperature. This can cause severe damage of the surface .The CHF is also referred to as a limit heat flux for this reason. The value of the critical heat flux is affected by hydrodynamic instabilities, wetting criteria, heat capacity, heater geometry, heating method, and pressure. In the first theory of Zuber [20] the CHF is reached when the Helmholtz

instability appears in the interface of the large vapor columns leaving the heating surface. These vapor columns are assumed to be in a square array. For vertical liquid and vapor flow, the critical Helmholtz velocity is (according with Kelvin-Helmholtz instability theory):

$$u_c = |u_l - u_v| = \sqrt{\frac{\sigma 2\pi}{\rho_l \lambda_D}} \qquad\qquad (2.10)$$

if $\rho_l \gg \rho_v$, λ_D is the wavelength.

Since the density of the vapor is significantly lower than that of the liquid, the upward vapor column velocity is much higher than the downward liquid velocity. Therefore, the critical Helmholtz velocity can be written in this second form:

$$u_c = \frac{q''_{max}}{\rho_v \lambda_D} \frac{A_S}{A_c} \qquad\qquad (2.11)$$

A_s total surface area A_c surface are occupied by vapor. The spacing of the centerline of the vapor column is λ_D and the diameter of the vapor column is supposed $\lambda_D/2$, the ratio A_s/A_c is equal to $16/\pi$ (see Figure 9).
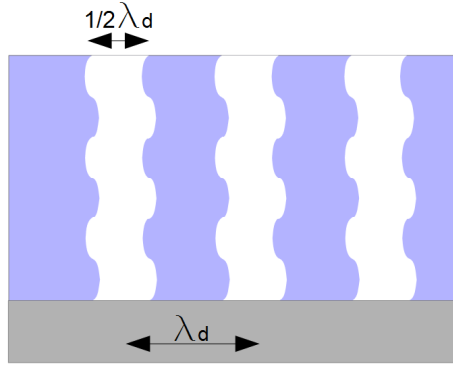
Figure 9: sketch of the vapor column (diameter and distance)

Combining the two form of the critical velocity, the critical heat flux is obtained:

$$q''_{max} = \frac{\pi \rho_v h_{vl}}{16} \sqrt{\frac{2\pi\sigma}{\rho_v \lambda_D}} \qquad (2.12)$$

According with [21] the most dangerous wavelength in the two-dimensional wave pattern for the Taylor instability of the interface between a horizontal semi-infinite liquid region above a layer of vapor:

$$\lambda_D = 2\pi \sqrt{\frac{3\sigma}{(\rho_l - \rho_v)g}} \qquad (2.13)$$

the critical heat flux becomes:

$$q''_{max} = 0.149 h_{vl} \left[\frac{\sigma g(\rho_l - \rho_v)}{\rho_v{}^2}\right]^{1/4} \hspace{3cm} (2.14)$$

The next two paragraphs present a brief review of methodology to improve these three boiling parameters (T$_{ONB}$, HTC, CHT) by the modification of surface topology (from macro to micro and even nanoscale). Conversely the wettability effect, that is the concerned effect studies of this work, is analyzed in the paragraph 2.5 .

2.3 Enhancement of pool boiling heat transfer by macro topology modification

The surface capability to entrapment of vapor/gas in a cavity is able to reduce the superheat temperature (ΔT_{sh}) necessary to activate nucleate boiling. Building reentrant cavities on the surface seems a prominent method to reduce the ΔT_{sh}, and it was one of the first used. Deng et al. [22] proposes a porous structures with reentrant cavities (Figure 10), constructed by sintered copper powder via a solid-state sintering method.
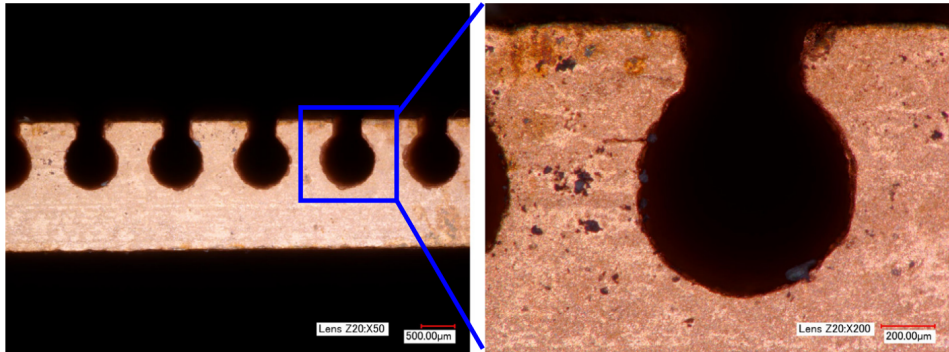
Figure 10: Solid copper structures with reentrant cavities [22].

In the both liquid tested (water and ethanol) a reduction of the T_{ONB} (up to 8-10°C less than smooth copper surface) can be found. The energy for the bubble nucleation and growth can be greatly lowered down in a cavity, and the ONB occurred at smaller heat fluxes.

The better performance of a reentrant cavities on comparison with no-reentrant cavity is shown also by Saha et al. [23]. They tested various types of tunnel structures (with hundreds of micrometers width, Figure 11) on copper surfaces using the wire EDM technique, and conducted water pool boiling experiments. The interest of this study is to investigate the enhancement of boiling heat transfer for different geometry of the channels.
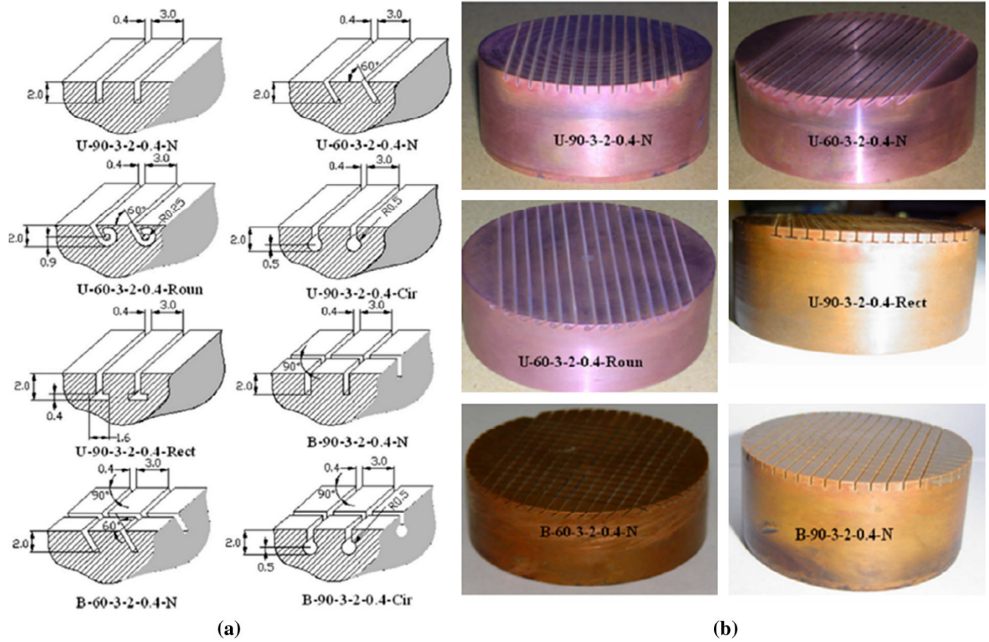
Figure 11: Various tunnel geometries (a) and views of test surfaces (b) [23].

Outcome of this work indicates that a tunnel with circular groove at the tunnel base could be an excellent option for the augmentation of boiling heat transfer. A reentrant cavity seems increase the heat transfer coefficient during nucleate boiling, decreases incipient superheat and enhances critical heat flux [24].

The creation of interconnections between the groves shows also benefit especially in term of CHF. Zhong et al. [25] interconnected-grooves surface with quadrilateral array and triangular array cavities (Figure 12). In this kind of structured surfaces, an excellent liquid vapor conversion system is formed. The cavities act as the stable cavity-centric vaporization cores and the interconnected grooves work as a cooling water supply pathways, which results in significant boiling heat transfer enhancement. The wall superheat reduction for given heat fluxes and CHF increases up to 60% for quadrilateral array and 102% for triangular array, compared with the plain surface.
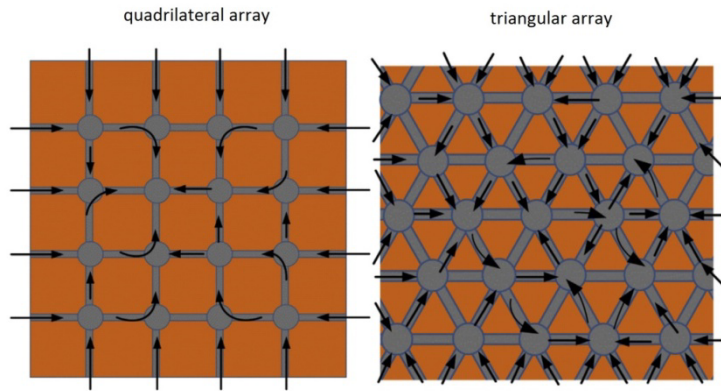
Figure 12: Schematic of fresh water motion around the structures [25].

A natural evolution of interconnected-grooves on a surface is the porous structure. Recently Xu et al [26] investigate the saturated pool boiling of

de-ionized water on composite porous surfaces. The porous layers contemplate three types of structures, including macro pores above 200 µm diameter, micro pores around 2 µm diameter and dendritic structure around 400 nm diameter. The porosity (percentage of void spaces in the material) of the coating layers varies from 91% to 94%. The experiment indicates that the micro pores and dendritic structure increases nucleation site density and capillary force, meanwhile, the macro pores contribute to the growing and departing of the bubbles. The highest heat transfer coefficient of the porous surface is in excess of 5.9 $W/(cm^2 K)$, 120% higher than for a plain surface. During high heat flux range, the coalescent bubble on the composite porous surfaces grows more quickly than plane surface, which brings more liquid replenishment after bubble departure, resulting in a higher CHF value. The highest critical heat flux of the porous surfaces reaches up to 239 W/cm^2, 101% higher than that of plain surface. The influence of the pore structure at microscale (less than about 100 µm) is likewise important on pool boiling phenomena, as explain in the next paragraph.

2.4 Enhancement of pool boiling heat transfer by micro-topology modification

This paragraph presents most of the technique used to enhance the pool boiling heat transfer efficient by surface modification at micro/nano-scale (less than about 100 μm). Over the past decades, researches on surfaces coated with various materials were actively conducted with the aim of enhancing boiling heat transfer [27]. The easiest way to modify a surface for this purpose is to introduce a roughness. The surface texture, on the other hand, is geometric in nature and can have many variables, such as pitch (periodicity), spacing, depth, shape, and randomness. In one of the first study about rough surface in nucleate boiling condition [28] it is shown how increasing the roughness reduce the ONB temperature. Increased surface roughness gives also better heat transfer at a given superheat [29] because the rough surface has usually more cavities than the smooth surface, while pool boiling heat transfer coefficient depends on the nucleation site density. In [30] Jones et al. pool boiling at atmospheric pressure from surfaces with a wide range of surface roughness (from 0.027 μm up to 10 μm) was been studied in two different fluids (water and FC-77). For water, the results indicate a little improvement in heat transfer coefficient for roughness beyond Ra =1.08 μm, except for a very rough 10.0 μm surface, which had significantly higher heat transfer coefficients. On the same set of surfaces, FC-77

exhibited a different trend with continuously increasing heat transfer coefficient with respect to surface roughness. The general trend of increasing heat transfer coefficient with surface roughness was correlated using $h \sim R^m$ (with m=0.2 for FC-77 and m=0.1 for water. In the recent work of Kim et al. [31] the effectiveness of micro-structured surfaces (circular micro-pillar arrays with height, diameter and gap between 5–40 μm) in enhancing the achieved HTCs and CHFs is investigated.

Sample No.	d (μm)	h (μm)	g (μm)	Roughness (r)	Solid fraction
S0	–	–	0	1	1
S01 (D20H10G05)	20	10	05	2.00	0.50
S02 (D20H10G20)	20	10	20	1.39	0.20
S03 (D20H10G40)	20	10	40	1.17	0.09
S04 (D20H20G05)	20	20	05	3.01	0.50
S05 (D20H20G20)	20	20	20	1.79	0.20
S06 (D20H20G40)	20	20	40	1.35	0.09
S07 (D20H40G05)	20	40	05	5.02	0.50
S08 (D20H40G20)	20	40	20	2.57	0.20
S09 (D20H40G40)	20	40	40	1.70	0.09
S10 (D05H20G05)	05	20	05	4.14	0.20
S11 (D05H20G10)	05	20	10	2.40	0.09
S12 (D05H20G20)	05	20	20	1.50	0.03

a)   b)

Figure 13: SEM image of prepared micro structured surfaces [31]

A roughness factor r, defined as the area fraction of the actual value (A_t) over the projected value (A_b), is used to evaluate the effect of roughness (Figure 14).

$$r = {A_b}/{A_t}$$
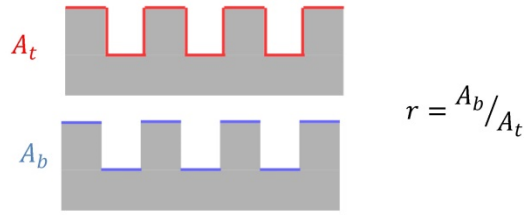
Figure 14: definition of roughness factor r.

The results HTC and CHF are dependent on the roughness factor, as shown in Figure 16a. At low superheat regime (before the ONB), the HTC showed no dependency on the sample roughness, since there is no bubble generation before the ONB. The thermal boundary layer (typically 100 µm Figure 15a) of the natural convection regime is greater than the structure's height (10–40 µm). So the structure could not affect the heat transfer rate.
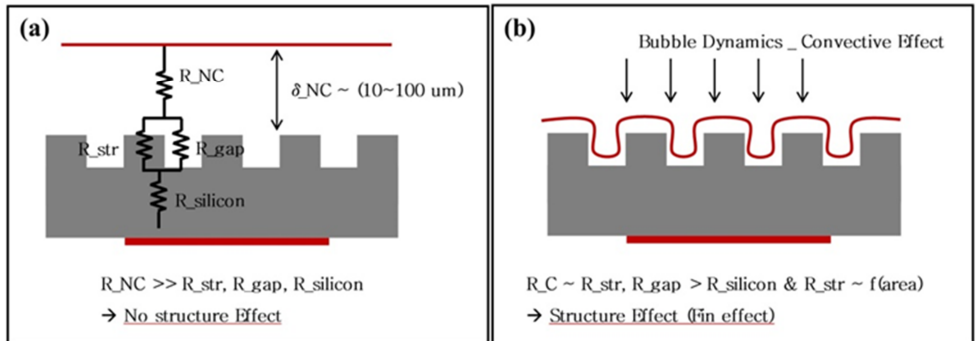
Figure 15: Thermal boundary characteristics a) before ONB b) at high superheat [31].

29

At higher superheat temperature (Figure 15a) the nucleated bubble behavior strengthened convection effects, affecting the thermal boundary layer. As the depth of the thermal boundary layer thickness has the same order of magnitude of the structure's height, there is an increase in the HTC due to the enhanced convection effects on the heating surface.
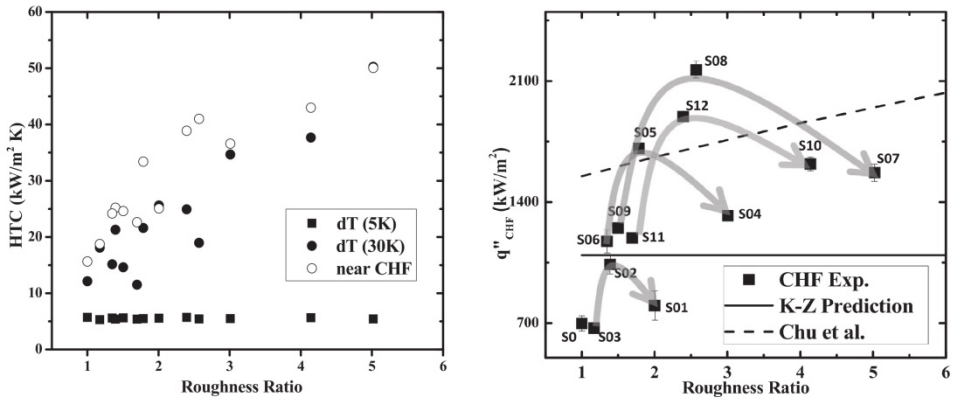
Figure 16: Boiling performance evaluation along the surface roughness ratio; (a) heat transfer coefficient, and (b) critical heat flux [31]

The trend of the CHF with roughness ratio is more complex (Figure 16b). It seems that, at fix height and diameter of the pillars, there is an optimal

gap size for CHF enhancement. This optimum value increases if the height of the pillar increase.

Finally many authors show that even nanoscale structures (size<0.1 micron) have an influence on pool boiling heat transfer. In Lu et al. [32] boiling experiments are conducted on a nano-porous copper surface (uniform porosity with approximately 30–200 nm). It is found that on the nano-porous surface more active nucleation sites are present. The nano-porous structure, as the micro-cavities at microscale, seems to reduce the activation energy for the bubble nucleation, giving a lower wall-superheat for the ONB in contrast with flat surfaces under the same heat flux conditions, as observed also in [33]. In Bourdon et al. [34] it is explained that the mean valley depth parameter S_v, a parameter to characterize the roughness, is able to quantify the sizes of the cavities present on the surface, and so estimate the importance of the nano-cavity on T_{ONB} reduction. As conclusion of these two paragraphs, a technique to enhance the pool boiling heat transfer should consider the following points:

> Increase in the active nucleation site density with randomly formed micro/nano-sized roughness and using reentrant cavities.

> Favorable bubble initiation, growth, and departure on microporous layered surface (reduce the bubble departure diameter).

> ➢ Promotion of evaporation mass flux at vapor–liquid interface by micro/nanostructures (roughness surface).

> ➢ Control the nucleation position, in order to delay the bubble coalescence and the formation of a vapor film (increase of critical heat flux).

Even the modification of surface wettability can help to achieve most of these points, as it is discussed in the next paragraph.

2.5 Enhancement of pool boiling heat transfer by surface wettability modification

The wettability is usually characterized by a contact angle. The cohesive forces between molecules of the same phase (liquid, solid and gas/vapor) are responsible for the surface tension. In the case the fluid is in contact with a solid surface, the equivalent forces between liquid and solid molecules is called interfacial tension. The equilibrium of the forces acting on liquid–vapor interface meets a solid surface determines the equilibrium contact angle (Figure 17).
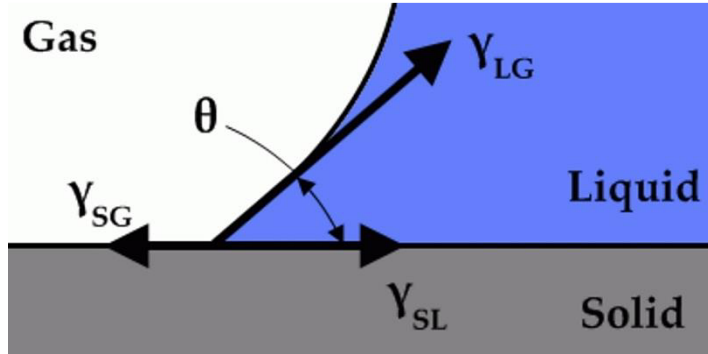
Figure 17: distributed forces at the contact line, with the contact line perpendicular to the image.

In the equilibrium, a contact angle of liquid drop on a surface can be described by the following Young's equation:

$$\gamma_{SL} + \gamma_{LG} \cos(\theta_e) = \gamma_{SG} \qquad (2.15)$$

Where $\gamma_{SL}, \gamma_{LG}, \gamma_{SG}$ are the interphase energy (N/m) between solid-liquid, liquid-gas and solid-gas. Application of this equation is limited to an ideal surface that is rigid, perfectly flat, insoluble, non-reactive, and chemically homogenous.

A high contact angle indicates a low solid surface energy or chemical affinity. This is also referred to as a low degree of wetting. The wettability of a surface can be modified by engineering its texture and (or) its chemistry. Basic on young equation the spreading parameter S is defined as:

$$S = \gamma_{SG} - (\gamma_{SL} - \gamma_{LG}) \qquad\qquad (2.16)$$

When S>0 a liquid droplet will completely wet the surface ($\theta_e = 0°$). This happens on a surface with very high value of γ_{SG} ($\sim 5 - 50 \ N/m$) as on the metal surface. When S<0 a liquid droplet a liquid droplet will partially wet the substrate: if $\theta_e \leq 90°$ a substrate is called hydrophilic and if $\theta_e > 90°$ a substrate is called hydrophobic. This hydrophobic regime is usually observed on substrates which have lower values of γ_{SG} ($\sim 0.010 - 0.050 \ N/m$) e.g. plastics. Some well-known surface chemistry method to modify the surface wettability include:

➤ forming oxides on the surface, if hydrophilicity is desired, For hydrophilic oxides (e.g., copper oxide), the chemistry and resulting wettability can be tuned by varying the degree of oxidation of the surface [35].

➤ depositing low-surface energy materials (e.g., fluoropolymers, fluorosilanes) if hydrophobicity is desired. The chemical bonds in low-surface energy solid materials are in order of decreasing surface energy: $-CH_2 > -CH_3 > -CF_2 > CF_2H > -CF_3$ (i.e., CF_3 is the least wettable) [36].

The wettability is function also of the surface texture. Wenzel [37] and Cassie and Baxter [38] describe the effect of the surface texture on value

of contact angle as consequence of two different state. Wenzel state assumes that the droplet completely wets the rough surface whereas Cassie and Baxter state assumes that air is trapped in the rough solid-liquid interface (Figure 18).
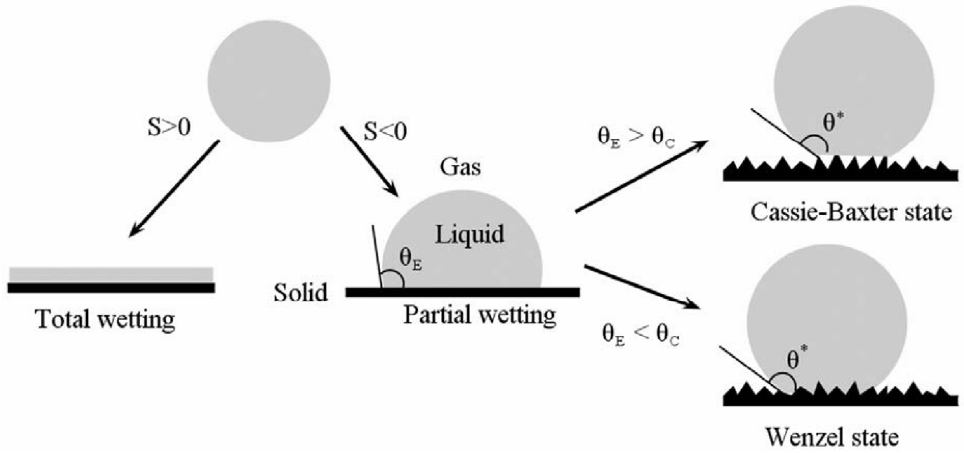
Figure 18: Possible wetting states of a sessile liquid droplet on a flat substrate, in function of spreading parameter and equilibrium contact angle. On Wenzel state, the droplet wet the substrate, in Cassie-Baxter state small gas pockets are located under the droplet.

In the real case both states can be present. In the Wenzel wetting state the apparent contact angle (θ^*) is function of the equilibrium contact angle on smooth surface:

$$\cos(\theta^*) = r \cdot \cos(\theta_e) \qquad\qquad (2.17)$$

with r being the roughness, defined as the ratio of the true surface area to the projected surface area. The possible cases are summarize in Figure 19:

➤ The **Cassie-Baxter partial wetting state** if $\cos(\theta_e) < \cos(\theta'_c)$ with $\theta'_c = (1 - \phi_S)/(r - \phi_S)$, where ϕ_S is the solid-liquid fractional surface area. The value of the apparent Cassie-Baxter contact angle is:

$$\cos(\theta^*) = 1 + \phi_S \left(\cos(\theta_e) - 1\right) \qquad (2.18)$$

➤ The **Cassie-Baxter non-wetting state** if $\cos(\theta_e) > \cos(\theta''_c)$ with $\theta''_c = (\phi_S + 1)/(r - \phi_S)$. The value of the apparent Cassie-Baxter contact angle is:

$$\cos(\theta^*) = -1 + \phi_S(\cos(\theta_e) + 1) \qquad (2.19)$$

➤ The **Wenzel state** $(\cos(\theta''_c) < \cos(\theta_e) < \cos(\theta'_c))$. The value of the apparent Wenzel contact angle is given by eq. (2.17).
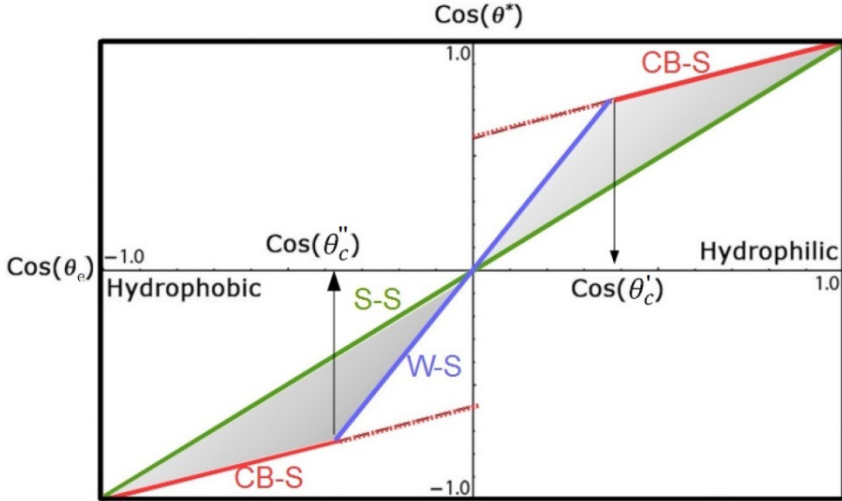
Figure 19: $\cos(\theta^*)$ in function of $\cos(\theta_e)$ for Wenzel state (in blue) and Cassie-Baxter state (in red).

The roughness is not important only on equilibrium contact angle but also for the so-called contact angle hysteresis (difference between the advancing[1] and receding[2] values). Advancing and receding contact angles are measured as a function of the roughness of a wax sample with constant chemical properties. Johnson and Dettre [39] study the advancing and receding contact angles as a function of the roughness of a

---

[1] The advancing angle between a liquid and a solid is the contact angle which is produced in the course of a wetting process.

[2] The receding angle is the contact angle between a liquid and a solid which has already been wetted with the liquid and which is in the course of being de-wetted

wax sample. The main outcome of the experiment is that an increase in the roughness caused an increase of the advancing contact angle and a decrease of the receding angle (so the hysteresis angle, which is the difference between advancing and receding, increases) until a limit value. At this limit, the hysteresis drastically decreased and the receding angle became closer to the advancing contact angle.

The whole pool boiling process is influenced by wettability properties. In L.W. Fan et al. [40] the effect of surface wettability on transient pool boiling, from the super-hydrophilic to the super-hydrophobic range is studied, using a quenching method with hot stainless steel spheres. The wettability is changed, with an equilibrium contact angle ranging from nearly 0° to more than 160°, by nanostructured coating on the spheres. The CHF for the super-hydrophilic case is found to increase by nearly 70%. The effect of the surface super-hydrophilicity is to destabilize the vapour film, helping the rewetting of the boiling surfaces even at high wall superheats. On the other hand, the super-hydrophobicity tends to reduce the T_{ONB}, although in default of specific micro-structured topology. In Bourdon et al. [41] the effect of wettability on the ONB is studied systematically, on the same nano-metrically smooth surface. By grafting with different monolayers of molecules, equilibrium static contact angle is changed from $0° < \theta_e < 110°$ without changing the surface topography. A non-linear decrease of the ONB with an increase of θ_e is observed. Even on a super-Hydrophobic surface ($\theta_e > 150°$), using

the same experimental apparatus in [42], it is shown a significant low temperature of T_{ONB} ($T_{ONB} \approx 2°C + T_{sat}$) on super hydrophobic surface. The first small bubbles are formed even when the surface has a temperature lower than the water saturation temperature. Similar results is reported by Takata et al. [43]. However in the case of a super-hydrophobic surface a quasi-Leidenfrost regime appears [42]. The formation of the vapor film on super-hydrophobic surface hinders to have high value of CHF. The effect of wettability on HTC is more complex. More recent studies also shows that hydrophobic surfaces enhance HTC by increasing the number of nucleation sites [44] and the bubble frequency due to the reduction of the waiting time [45] . The recent study of Jo et al. [45] about boiling on smooth silicon samples, showed that a hydrophobic coating ($\theta_e = 123°$) enhance the HTC by a factor up to 3 compared to a hydrophilic coating ($\theta_e = 54°$). It is possible to conclude that hydrophobic surfaces had an onset of nucleate boiling at superheats lower than hydrophilic ones, but super-hydrophobicity induces stable film boiling at very small values of superheat (as shown in [46]). Based on these experimental observation, the relative improvement of T_{ONB} and CHT can be obtained by a biphilic surfaces: a surface with disperse small hydrophobic regions to promote nucleation surrounded hydrophilic regions, to prevent early CHF. Experiments have shown that biphilic surfaces actually enhance the heat transfer performances (HTC and CHF) in pool boiling. In Betz et al. [47] the biphilic surface is tested in pool

boiling condition. They investigate the effect of the biphilic surface on HTC, by varying the diameter of the hydrophobic spots, at constant pitch to diameter ratio. Experiment show that at low superheat, the 400 µm spots induce higher HTC, while at larger superheat, the 50 µm spots induce higher HTC. This can be explained by the fact that at low superheat the bubbles released from the 400 µm spots are larger, while at higher superheat the surface with 400 µm spots offers less nucleation sites than the surface with smaller spots.

The size and pitch distance between hydrophobic dots are the key parameters for explaining boiling performance under heterogeneous wetting conditions:

➢ At **low heat flux**: the effects of dots size and pitch distance are important. The HTC is enhanced as the hydrophobic dot diameter increases. We conjectured that this variation is caused by reduction of T_{ONB} for bigger dot diameters. The HTC is improved as the pitch distance decreased. The reduction of the pitch distance increase the density of nucleation site on the surface.

➢ At **high heat flux**: The HTC is lower for bigger dots size. Indeed the continuous bubble generation interrupts heat transfer because part of the surface is constantly covered by vapor, and cannot be cooled by liquid rewetting, causing the HTC to decrease. As the pitch distance decreased, bubble interactions and coalescence

occurred more frequently, leading to shorter bubble growth time. Instead the departing diameter is more or less independent of the micro dot sizes used (50μm-500μm). Therefore, at high heat flux, high density hydrophobic dots (small dots and small pitch distance) could result in decreasing the value of the CHF.

Wettability could be influenced by the temperature. This is clearly important to estimate in the case of heat transfer in boiling condition. The effect of temperature on equilibrium contact angle is the object of the next paragraph.

2.6 Effect of temperature on equilibrium contact angle

The measurement of the equilibrium contact angle of a sessile drop becomes very challenging when the fluid temperature is close to the saturation temperature. Furthermore the equilibrium contact angle close to boiling conditions is an essential input parameter for numerical simulations capturing the heterogeneous phase change phenomena, like drop impact onto heated surfaces. Several groups have studied the effect of temperature on the equilibrium contact angles either experimentally, with direct measures, or numerically, using molecular dynamic simulations. However there is still a disagreement between the authors. For hydrophilic surfaces the experiments seem to show a reduction of the equilibrium contact angle with the increase of the surface temperature. In

Aydar et al. [48] contact angles of oils on polytetrafluoroethylene (PTFE) with different surface temperature (from 23°C up to reaching the oils' smoke point of 200°C) are measured and compared to values predicted by the Girifalco-Good-Fowkes-Young (GGFY) equation [49]. This equation, in combination with the Eötvös rule (that assumes a surface tension function linear with the temperature), predicts a reduction of contact angle with increase of the surface temperature (as shown in Figure 20).
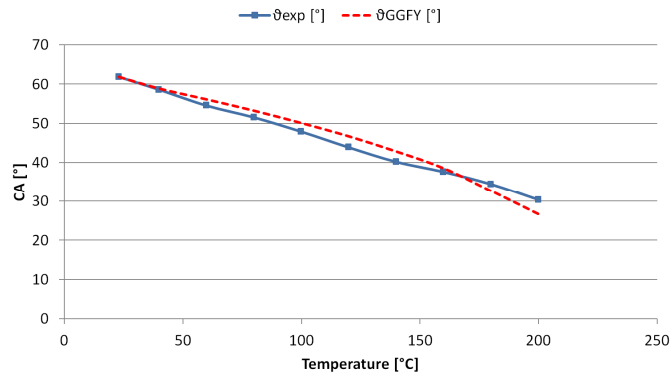
Figure 20: Comparison between equilibrium contact angles measurement of Canola oil on polytetrafluoroethylene (PTFE) In Aydar et al. [48] , using air as surrounding media, and Girifalco (GGFY) equation [48].

Petke et al. [50] measured the temperature dependence of contact angles of liquids on hydrophilic and hydrophobic plastic surfaces, stating that the ECA decreases with the surface temperature in both cases.

Although most of the existing literature predict a reduction of ECA with temperature, not all the authors agree with this trend. Kenneth et al. [51] examined surface temperature-dependence of the contact angle of water on graphite, silicon, and gold. The contact angle of water on various substrates do not monotonically decreases in every experiment, but also other behaviors (monotonic decrease of contact angle and no change in contact angle) have been observed. Kandlikar et al. [52] measured the CA during rapid evaporation of liquid on a heated hydrophobic surface and the values of the apparent CA for high surface temperatures (100 °C < T_w < 250 °C) are remarkably constant. The linear behavior of the surface tension of both water and diiodomethane is studied by Konrad et al. [53] using a temperature controlled monocrystaline quartz in the range 5–50°C with temperature steps of 5°C. They show that the liquid temperature has a much larger effect on the value of contact angles for polar liquids (water) than for apolar liquid (Diiodomethane). Recently Stock et al. [54] using an AFM (Atomic-force microscopy) measurement show that, on hydrophobic surfaces, the adhesion force decreases significantly by 20% increasing room temperature. Direct experimental measurements are performed in order to evaluate the variation of the equilibrium contact angle with temperature. The apparatus used to measure the equilibrium contact angle is schematically described in Figure 21. A drop shape analyzer (DSA100-Kruss©) is used to measure the contact angle of a sessile drop on the selected surface. The sample and the syringe are

connected to a thermal bath (Julabo© EC-5) in order to change the temperature of the system. An IR-camera (SC5000 Flir®) is placed on the other side of the chamber to measure the average temperature of the droplet for some preliminary tests. More detail about this experiment can be found here [55].
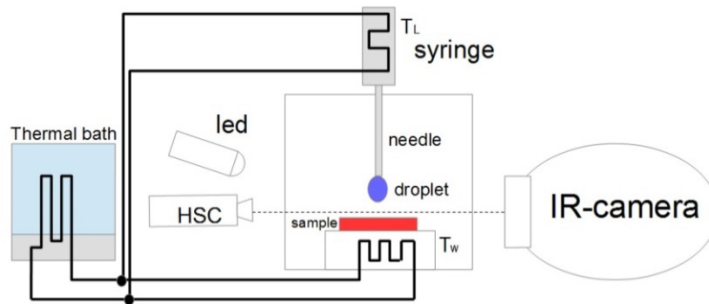
Figure 21. Sketch of the experimental set-up.

Table 1 reports the equilibrium contact angle (measured at ambient temperature of 20°C) for the three considered surfaces (Aluminium, PTFE, glass sample with a thin coating to generate super-hydrophobicity using the commercial product Glaco Mirror Coat Zero©). All the surfaces can be considered smooth (R_a<0.2 µm). In the measurement of the equilibrium contact angle, the experiment is conducted in an environment with 3 species (solid material, water and air) at ambient condition ($P_{chamber}$ = 1Bar and $T_{chamber}$ = 20°C). The presence of air and the no saturation

condition of the gas phase (vapor and air) can induce inaccuracy on the equilibrium contact angle measurement. As reported by Weisensee et al. [56] on a flat Teflon-coated surface, the static contact angles could be slightly lower in the water vapor environment than in air. Another issue is the high temperature of the sample surface causes the evaporation of the droplet, reducing the contact angle.

Table 1. Equilibrium contact angle of the surfaces, at temperature $T_0=20°C$, measured with sessile drop method (liquid is water). The mean roughness (R_a) of the surface is also reported.

Surface	Equilibrium contact angle [°]	Ra [µm]
PTFE	110.6 ± 2.2	0.188
Aluminium	68.6 ± 5.0	0.135
SHS	148.6 ± 3.6	0.062

Table 2 presents the physical properties of the tested liquids. Though the study is focused on water liquid behavior, also two other liquids (ethanol and isopropanol), with lower surface tension, are tested. Table 2 shows interesting physical properties of the three tested liquids.

Table 2. Physical properties of the three liquids tested. T_{sat} is the boiling temperature (at 1 atm). Surface tension, density and dynamic viscosity are evaluated at T_{sat} for each liquid.

	Water	Ethanol	isopropanol
T_{sat} [°C] – 1 atm	100	78.37	82.6
Surface tension [mN/m]	58.81	17.41	15.98
Density [Kg/m³]	973	733	727
Dynamic viscosity [mPa*s]	0.283	0.420	0.522

Figure 22 shows the evolution of the apparent contact angle (DCA) for a water droplet on aluminium (Figure 22a) and PTFE (Figure 22c). The evaluation of what we have defined as "equilibrium contact angle" (ECA) will take place in the equilibrium phase (t1<t<t2) as average of the apparent contact angles during this period (eq. 3.16):

$$\theta_{CA} = \frac{\int_{t1}^{t2} \theta_{DCA}(t)}{t2 - t1} \qquad (2.20)$$

The variation of the contact angle in this stage is essentially due to the droplet evaporation while the contact line CL is almost constant due to the drop pinned. CL is the footprint of the projected drop profile, recorded by HSC. Figure 22b and Figure 22d show that up to t = 50s the CL doesn't change. Using the values t_1=2s and t_2=6s to define the equilibrium

range, on the aluminium surface (Figure 22a) with $T_w=50°$ and $T_w=70°C$, the CA changes up to $3°$, while on the PTFE (Figure 22c) the variation of the apparent contact angle is negligible, probably due to the higher evaporation rate.
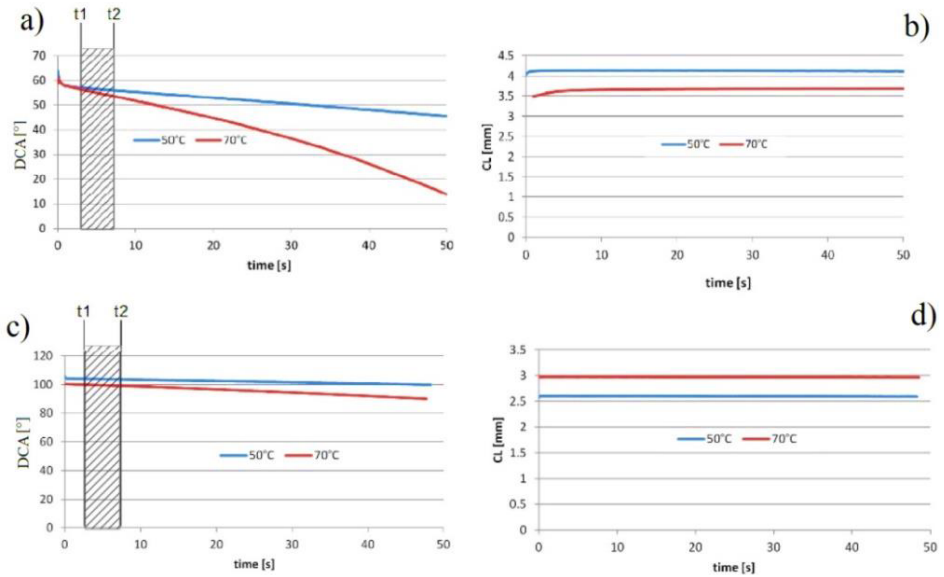
Figure 22: a) evolution of the apparent contact angle of a water droplet on aluminium; b) contact line (CL) evolution of a water droplet on aluminium; c) evolution of the apparent contact angle of a water droplet on PTFE; d) contact line evolution of a water droplet on PTFE.

Using the values $t_1=2s$ and $t_2=6s$ to define such "equilibrium phase", the ECA is therefore evaluated for water on Teflon and aluminium (In Figure 23) using equation (7). A clear decrease appears for the hydrophilic

aluminium sample (from 70.3° to 58.5°), the standard deviation in this measurements is between 5° and 7°. Also on the hydrophobic PTFE sample a slight decrease appears (from 109.5° to 101.0°), however the uncertainty on the calculation of equilibrium contact angles (a standard deviation of 7° is reached at higher temperatures). For SHS coating, the ECA is almost constant (from 148° to 151°) considering the standard deviation (4°) of the calculation. Two other liquids (ethanol and isopropanol) are also tested on PTFE surface. A decrease of the equilibrium contact angle can be observed in both cases. Figure 24 a shows the decreasing of the ECA with temperature (from ECA=35.3° to ECA=27.7°) for ethanol. Similar trends can be found for isopropanol (from ECA=31.3° to ECA=21.1°). In this case the standard deviation is around 5°.
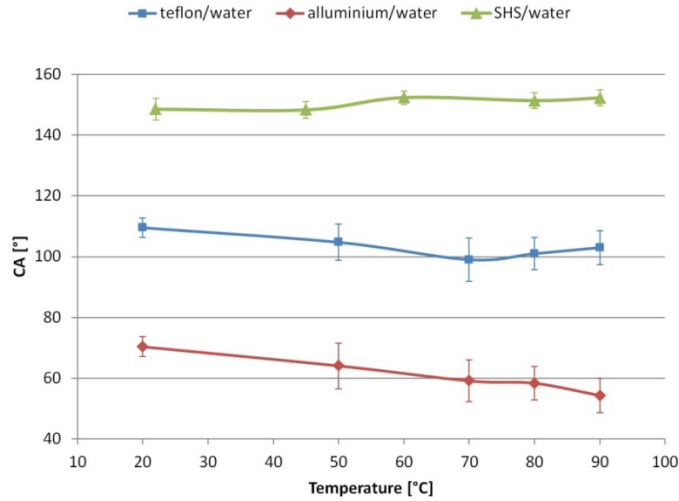
Figure 23: a) Evaluation of the equilibrium contact angle at different temperature for a water droplet on Aluminium, Teflon and SHS.
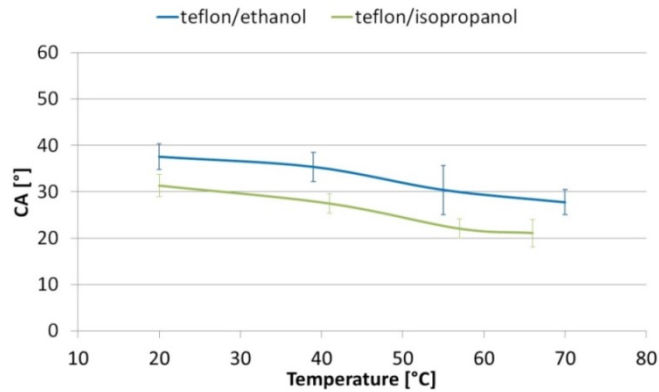
Figure 24: Evaluation of the equilibrium contact angle at different temperature of an ethanol and isopropanol liquids on PTFE.

Chapter3

3 phase change simulation

3.1 Introduction of two phase flow simulation

Nowadays the increasing of the computing capabilities permits the simulation of complex multiphase-phase flows, as in the case of numerical simulation of boiling heat transfer. Computational Fluid Dynamics (CFD) codes are the commonly tools for a fluid-dynamic simulation. In the recent years, the use of CFD codes has been extended to the analysis of three-dimensional multi-phase flows, aiming to overcome the weakness of 1D numerical models. Up to present, two main branches exist in the literature for the numerical investigation of boiling heat transfer using CFD [57]. The first one has adopted a Eulerian multiphase flow approach, based on a two-fluid model. In this approach, it is necessary to include phase interaction terms as sources/sinks in the governing equations that are depending on specific problem. These

additional terms require empirical relations to predict e.g. the bubble departure characteristics or the density of the active nucleation sizes. The empirical relations, since they incorporate a number of model constants, are depending on specific flow conditions. Recently, in the work of Prabhudharwadkar et al. [58] and Cheung et al. [59] the performance of a wide combination range of the existing closure relationships is examined through comparison with a wide range of experimental data. The second branch approach is a complete or "direct" numerical simulation of the complex spatial and temporal evolution of the interface between the two phases, utilising a variety of interface tracking/capturing approaches (Figure 25):
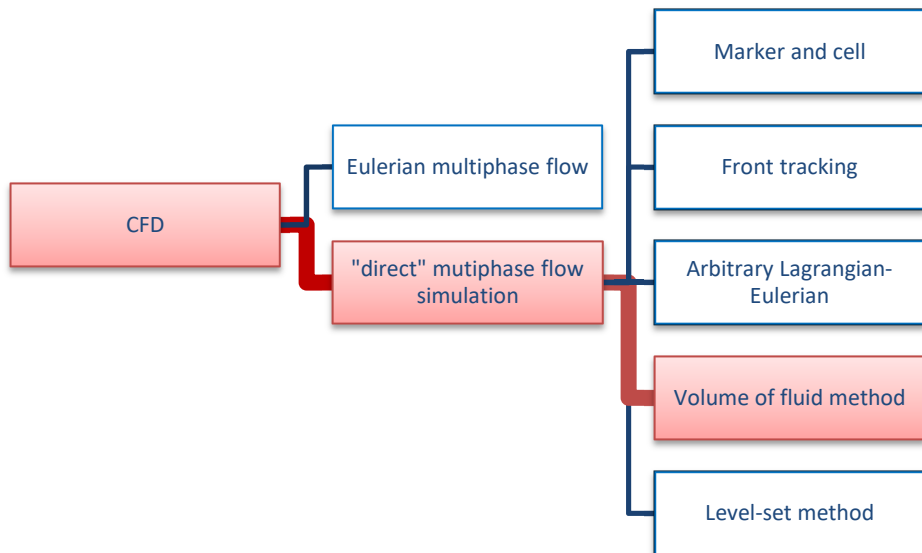
Figure 25: fluid-dynamic approaches for a phase change numerical analysis. In red is highlight the approach choose in this work.

➢ **Marker and Cell** (MAC) method [60]: the interface is marked by many weightless particles that are convectively transported with the calculated velocity field. The particles are used to reconstruct the interface position on a fixed mesh.

- ➢ **Front tracking** (FT) method [61]: The interface is tracked by a Lagrangian frame and its position can be tracked precisely.

- ➢ **Arbitrary Lagrangian-Eulerian** (ALE) method [62]: In this method a dynamic mesh follows the motion of the interface, so the interface coincides with a boundary of the computational domain at each time instance during the computation.

- ➢ **Volume-of-Fluid** (VOF) method [63]: this method calculates a field (alpha) that contains information about the volume fraction of one of the phases in a numerical cell and which is convectively transported with the velocity field. The volume fraction field is used to evaluate the position of the interface.

- ➢ **Level-Set** (LS) method [64]: this method calculates a function that contains information about the distance of each computational cell to the interface. This function is convectively transported with the velocity field. The zero-isoline of the level-set function is the interface position.

The Volume-of-Fluid (VOF) method is used in this work to simulate the pool boiling phenomena. The proposed method constitutes an enchanced VOF method that has been developed in the past in the general context of OpenFOAM CFD Toolbox. The proposed method is briefly described in the following paragraphs. Further details regarding the particular

enhancements in the original VOF method of OpenFOAM can be found in the following works .

3.2 Adiabatic VOF method

In the VOF approach, a single set of continuity (equation 4.1) and Navier–Stokes equations (equation 3.2) for the whole flow field is solved simultaneously with a transport equation for the volume fraction (equation 3.3), called α, of the secondary (dispersed) phase. The corresponding volume fraction of the primary phase is calculated as (1-α). The main assumptions are that the two fluids are Newtonian, incompressible, and immiscible. The set of equations can be written as:

$$\nabla \cdot (\rho \vec{U}) = 0 \tag{3.1}$$

$$\frac{\partial (\rho \vec{U})}{\partial t} + \nabla \cdot (\rho \vec{U}\vec{U}) - \nabla \cdot \{\mu[\nabla \vec{U} + (\nabla \vec{U})^T]\} = -\nabla p + \vec{f_g} + \vec{f_{ST}} \tag{3.2}$$

$$\frac{\partial \alpha}{\partial t} + \nabla \cdot (\alpha \vec{U}) = 0 \tag{3.3}$$

where $\vec{U}$ is the fluid velocity vector, p the pressure, ρ the fluid density, μ the bulk dynamic viscosity, $\vec{f_g}$ the gravitational force field, and $\vec{f_{ST}}$ the volumetric representation of the surface tension force. The bulk density ρ and viscosity μ are computed as the averages over the two phases (l liquid, v vapor), weighted with the volume fraction α:

$$\rho = \rho_l \alpha + \rho_v (1 - \alpha) \tag{3.4}$$

$$\mu = \mu_l \alpha + \mu_v (1 - \alpha) \tag{3.5}$$

In this VOF method, for the case of incompressible flow, the volume fraction α is conserved. The surface tension force $\overrightarrow{f_{ST}}$ should be modelled as a volumetric force. A common method, called the Continuum Surface Force (CSF) by Brackbill et al. [65], applying the following equations:

$$F_S = \gamma k (\nabla \alpha) \tag{3.6}$$

where γ is the tension of the interface, $\nabla \alpha$ is the gradient of the volume fraction, and κ is the curvature of the interface.

$$k = \nabla \cdot \left(\frac{\nabla \alpha}{|\nabla \alpha|} \right) \tag{3.7}$$

3.3 Diabatic VOF method

The classical VOF is mass conservative (equation 3.1). The original formulation of VOF method n OpenFOAM doesn't have any model to take into account the phase change phenomena. However the classical VOF method in OpenFOAM can be modified to include the simulation of diabatic liquid-vapor flows with phase change. In the work of [57] the model proposed by Hardt and Wondra [66] is implemented in an already improved adiabatic VOF-solver of OpenFOAM, that has been previously treated accordingly for spurious currents suppression ([67], [68]). After

the proposed implementation [67], this new solver (Diabatic VOF-solver) has been quantitatively validated against an analytical solution for a growth of a spherical bubble in a superheated liquid domain using three different working fluids [69], for a single bubble growth and detachment during pool boiling[69], and flow boiling in a micro-channel [70]. The accordingly modified governing equations are:

$$\nabla \cdot (\rho \vec{U}) = \dot{\rho} \tag{3.8}$$

$$\frac{\partial(\rho \vec{U})}{\partial t} + \nabla \cdot (\rho \vec{U}\vec{U}) - \nabla \cdot \{\mu[\nabla \vec{U} + (\nabla \vec{U})^T]\} = -\nabla p + \vec{f}_g + \overrightarrow{f_{ST}} \tag{3.9}$$

$$\frac{\partial(\rho c_p T)}{\partial t} + \nabla \cdot (\vec{u} \cdot \rho c_p T) - \nabla \cdot (\lambda \nabla T) = \dot{h} \tag{3.10}$$

$$\frac{\partial \alpha}{\partial t} + \nabla \cdot (\alpha \vec{U}) - \nabla \cdot (\alpha(1-\alpha)U_r) = \frac{\dot{\rho}}{\rho} \alpha \tag{3.11}$$

Compared to adiabatic VOF method, the equations are amended as follows:

➢ In the mass conservation equation (equation 3.8) a source term on the right hand side accounts for the phase change ($\dot{\rho}$). The mass is globally conserved despite local source terms since all of the mass that is removed from the liquid side of the interface is added on the vapor side.

➢ The momentum source terms (equation 3.9) in the right hand side of the equation account for the effects of surface tension and gravity, respectively.

➢ A new equation for the conservation of energy (equation 3.10) is added in the diabatic solver. The balance the source term on the right hand side of the equation represents the latent heat of evaporation ($\dot{h}$).

➢ In the equation for the volume fraction (equation 3.11), an extra compression term ($\nabla \cdot (\alpha(1 - \alpha)U_r)$) is introduced artificially to sharp the interface. Interface sharpening is very important in simulating two-phase flows of two immiscible fluids, because it reduces the numerical instability of the solver [71]. U_r is the artificial compression velocity which is calculated from the following relationship:

$$U_r = n_f \min \left[C_\gamma \frac{|\varphi|}{|S_f|}, \max \left(\frac{|\varphi|}{|S_f|} \right) \right] \qquad (3.12)$$

Where n_f is the cell surface normal vector, φ is the mass flux, S_f is the surface area of the cell, C_γ is the coefficient (here the value is set 1) that controls the level of compression ([71, 72]). U_r is the relative velocity between the two fluid phases due to the density and viscosity change across the interphase. The source term adds

on the right hand side ($\frac{\dot{\rho}}{\rho}\alpha$) is needed because, due to the local mass source terms, the velocity field is not free of divergence.

3.4 Phase change model

The Diabatic VOF method requires a model to evaluate the mass transfer due to evaporation. The model used is based on the work of Hardt et Wondra [66]. The quantity that should be estimated is the evaporating mass flux at the liquid–vapor interface j_{evap}. This term can be calculated from the following relationship:

$$j_{evap} = \frac{T_{int} - T_{sat}}{R_{int} h_{lv}}$$
(3.13)

where T_{int} is the temperature of the interface, T_{sat} is the saturation temperature, R_{int} is the interfacial heat resistance and h_{lv} is the latent heat of evaporation. The interfacial resistance is evaluated from following relationship [73]:

$$R_{int} = \frac{2-a}{2a} \frac{\sqrt{2\pi R_{gas}}}{h_{lv}^2} \frac{T_{sat}^{3/2}}{\rho_v}$$
(3.14)

R gas is the specific gas constant of the working fluid. The constant $"a"$ is taken equal to unity according with the literature [74].

Using the j_{evap} the mass source term for evaporating/condensation can be evaluated. This is done by multiplying the evaporating mass flux at the

liquid–vapour interface by the magnitude of the volume fraction gradient, as indicated in the following equation:

$$\dot{\rho}_0 = j_{evap}|\nabla\alpha| \tag{3.15}$$

This initial sharp source term field (SSTF) is integrated over the whole computational domain to calculate the "Net Mass Flow" through the entire liquid-vapour interface, using the following equation:

$$\dot{m}_{int} = \iiint_V \dot{\rho}_0 dV \tag{3.16}$$

The source term field, that it is initially concentrate on the interphase, is then smeared over several cells, by solving the following a diffusion equation for the smooth distribution of source terms:

$$\dot{\rho}_1 - \nabla \cdot [(D\Delta\tau)\nabla\dot{\rho}_1] = \dot{\rho}_0 \tag{3.17}$$

$\Delta\tau$ is an artificial time step. The width of the smeared source term field is proportional to $\Delta\tau\sqrt{D}$. $\Delta\tau$ and D values are adjusted to the mesh resolution such that the source term field is smeared over several cells (around 5). After that the cells that do not contain pure phase ($\alpha < 1$-α_{cut} or $\alpha > \alpha_{cut}$, with α_{cut}=0.05) are set to zero the source term, to ensure that source terms are transferred only into the pure vapor and liquid cells in the vicinity to the interface. The interface therefore is not subjected to any source terms. Therefore, the algorithm for the volume fraction field as well as the associated interface compression, can work efficiently without

any interference with the source term field. However the remaining source term field should be scaled individually on the liquid and the vapor side in order that the mass is globally conserved and that the evaporating or condensation mass flow, corresponds globally to the net mass flow through the interface:

These scaling coefficients N_l and N_v are calculated by integrating the smooth source term field in each of the pure phases and comparing it to the net mass flow, from these relationships:

$$N_l = \dot{m}_{int} \left[\iiint_V (\alpha - 1 + \alpha_{cut}) \dot{\rho}_1 dV \right]^{-1} \qquad (3.18)$$

$$N_v = \dot{m}_{int} \left[\iiint_V (\alpha_{cut} - \alpha) \dot{\rho}_1 dV \right]^{-1} \qquad (3.19)$$

Using this scaling factor the final source term distribution is evaluate in this way:

$$\dot{\rho} = N_v(\alpha_{cut} - \alpha)\dot{\rho}_1 - N_l(\alpha - 1 + \alpha_{cut})\dot{\rho}_1 \qquad (3.20)$$

More details regarding the proposal approached can be found in [57], [68].

Chapter 4

4 Pool boiling experiment

4.1 Experimental apparatus

The experiment apparatus, that it is also described in [75], used in this work to do pool boiling experiment is shown in Figure 26. The boiling chamber is made by aluminium. An internal heater (80W) is initially used to heat up the water. Moreover, three external heating tapes are placed on the walls chamber and they are connected to a PID controller in order to balance any potential thermal leakages. These external heating tapes work in conjunction with a cooling system (air coils places on the top of the chamber), to raise the temperature of the chamber and maintain the water saturation conditions inside the chamber (T_{ch}=100°C and P_{ch}=101.3 kPa). T_{ch} and P_{ch} are measured by a K-thermocouple and a piezo-electric pressure sensor, respectively. The sample is then heated up until the desired temperature, T_{wall} , by an 175 W, Acim© JouaninH6.5X32X175 heating cartridge. Finally a heat flux meter with 3 embedded T-

thermocouples is placed between the copper housing of the ceramic cartridge and the sample surface to provide a direct measure of the heat flux. All the thermocouples and the pressure gauge are connected to a PC through a data acquisition system, and the pool boiling process can be recorded, by an HCC-1000 high-speed camera (VDS Vosskuehler©, resolution of the images is 7,65 μm/pixel). The measuring accuracy of the T and K-thermocouples is 0.5 K, accuracy of the pressure gauge is 5 hPa.
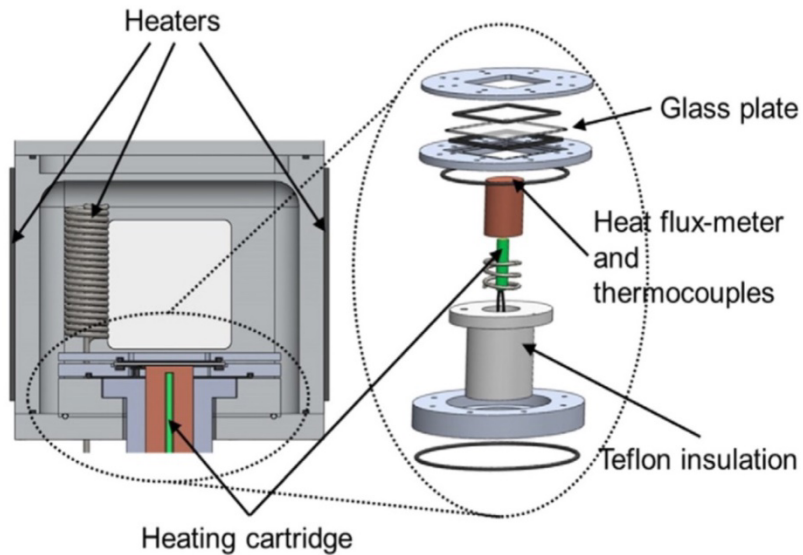
Figure 26: Schematic of the chamber.

The protocol used for each boiling experiment is performed is shown in Figure 27:

I. The vacuum inside the chamber is pulled using a vacuum pump, until a pressure of about 60 millibars, in order to remove a maximum of air and adsorbed gases (t_a).

II. A degases water starts to fill the chamber (t_b) until completely fills the box.

III. After the filling of the chamber, all the valves are closed. The pressure inside the chamber is equal to the atmospheric pressure and the water temperature is much lower than the saturation temperature of the water. The internal heater (Int heater in Figure 27) is then turned on to heat up the water close to its saturation temperature. When the temperature of the liquid is close to the saturation temperature, vapor bubbles are formed on the roof of the chamber, leading to an increase of the pressure. To keep the pressure (and thus the temperature) at the desired saturation condition (point t_c), the external air cooling system controls the steam to condense and avoids the variation of the pressure.

IV. When saturation conditions in a chamber are stable, the data acquisition starts (using a data acquisition/switch unit). The values of temperatures (T_w, T_{ch}) pressure (P_{ch}) and heat flux (W/m2) are recorded during all the experiment. Heating cartridge, that is placed under the sample, is switched on to increase the sample temperature . The boiling curve is then built from these data. A

high speed camera record the pool boiling phenomena when bubbles appear.
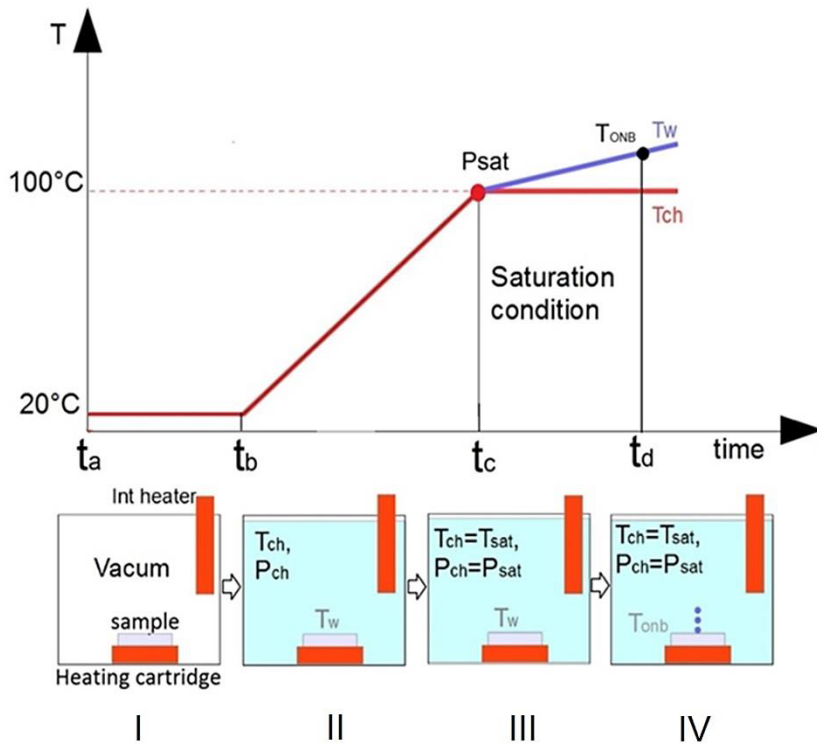
Figure 27: Pool boiling experimental procedure.

4.2 Effect of wettability

The wettability characteristics of the considered surfaces are summarized in Table 3. As mentioned previously, three different surface configurations are tested, using these characteristics:

➢ *HydroPhilic Surface (HPiS):* AISI 316 stainless steel sample, with no coating applied.

➢ *Super-Hydrophobic Surface (SHS):* the same sample HPS is covered by a uniform and thin coating to generate super-hydrophobicity using a commercial product (Glaco Mirror Coat Zero©)

➢ *Hybrid surface (SHS_D):* only a small circle (diameter 4.6 mm) in the center of the same sample HPiS is covered by the Glaco Mirror Coat Zero© coating, while the rest of the sample remains hydrophilic.

Table 3: Wettability properties of the considered surfaces. Equilibrium contact angle (θ_{eq}), advancing contact angle (θ_{adv}), receding contact angle (θ_{rec}) and hysteresis (θ_{adv}-θ_{rec} =$\Delta\theta$). The angles are measured using the sessile drop method. Maximum standard deviation is ±3°.

	θ_{eq} [°]	θ_{adv} [°]	θ_{rec} [°]	$\Delta\theta$ [°]
HPS	58	74	43	31
SHS	150	151	149	2

The roughness characteristics of the sample that is used in all the above surface configurations are summarized in Table 2. The mean roughness is quantified by the "Average Roughness" (Sa) and the "Root Mean Square Roughness" (Sq). As it is already shown in [34] the key parameter for the incipient boiling is not the mean roughness, but the peak-to-valley depth (Sz) or even better, the "mean valley depth" (Sv), which is able to quantify the sizes of the cavities that are present on the surface.

Table 4: Main roughness characteristics for the sample used. The reported roughness values have been measured using a confocal microscope (S neon-Sensofar©).

Roughness parameter	Value (µm)
S_a	0.046
S_q	0.063
S_z	0.989
S_v	0.416

In order to measure the dynamic apparent contact angles of the generated bubbles, a special post-processing routine has been developed within the general framework of Matlab© software:
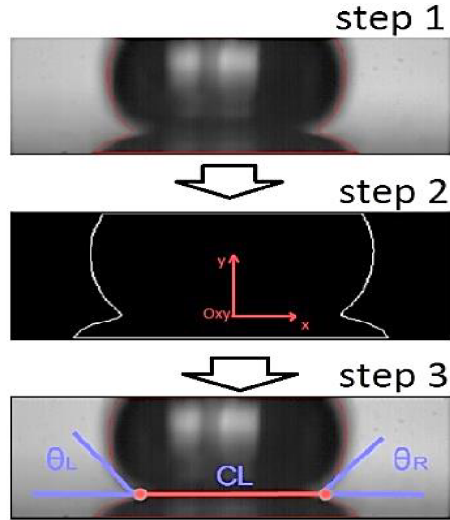
Figure 28: Post processing steps to measure the dynamic apparent contact

angles (θ_L and θ_R) and the apparent contact line (CL).

> **Step 1**: The proposed image processing procedure starts from the identification of the bubble boundary (Figure 28) and its digital automatic extraction to obtain the X and Y coordinates of the bubble boundary.

> **Step 2:** The frames are transformed from the grayscale image into a binary one. After the identification of the solid-liquid interface (the plane y=0) the position of the two points where the three

phases solid-liquid-vapour are in contact (in the 2D side view of the generated in each case bubble) is identified.

➢ **Step 3:** Using a parabolic interpolation (2nd order) for the shape of the bubbles close to these two points, 20 points are the selected number of point generate the proposed interpolation (a robustness tested of the image process is performed using different number of point from 5 to 30 in order to identified the optimum number of points). the apparent contact angles (θ_R and θ_L) are calculated, as the first order derivate of the parabola in the y=0 coordinate. The same image post processing procedure is also applied to the numerical simulation animations of the present investigation, in order to extract the numerically predicted angles.

The hydrophilic case result is shown in Figure 29. The first nucleation site appears at a wall temperature T_{ONB}=117°C. While the temperature of the wall increases, the numbers of nucleation sites increase (multiple boiling points) up to the formation of a vapor film on the surface.

The overall process for a single nucleation site on HPiS are divided into 4 main stages:

➢ *nucleation*, the generation of the bubble nucleus. At this point it should be mentioned that on the experiment we consider nucleation when the first small bubble is visible on the surface.

- ➢ ***bubble growth*** *phase* (due to phase change)

- ➢ ***bubble detachment*** phase

- ➢ ***waiting time*** phase (before the next nucleation event).

Figure 29: Hydrophilic case result. The pool boiling starts on HPiS surface at 117°C. On the bottom there is the bubble growth and detachment process on the tested surfaces in the experiments (Four stages are identified: nucleation, growth, detachment, waiting time.

In Figure 30a it is depicted the evolution of the contact line for a bubble on HPiS at different T_{wall}. The expansion rate of the contact line is much larger than the contraction rate. The t_{detach}, the time between the nucleation of the bubble and the detachment from the surface, depends primarily on these contraction rate. In Figure 30b there is the apparent contact angle for a bubble on HPiS at different T_{wall}. The apparent contact angle (θ_{app}) remains in the range $\theta_{adv} < \theta_{app} < \theta_{rec}$ during the bubble growth process (at higher tested temperature $T_w=123°C$ seems lower then θ_{rec} for t<3ms).
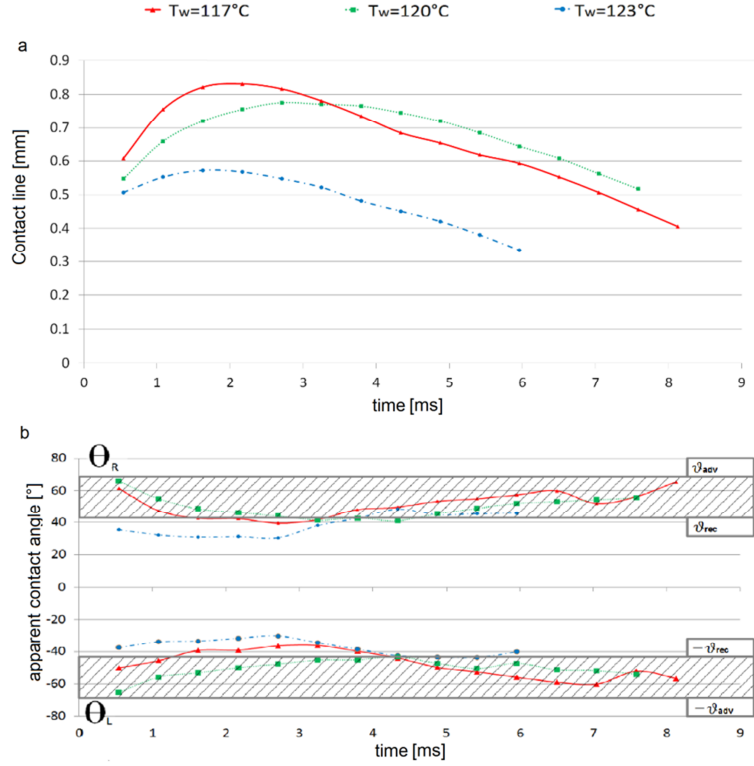
Figure 30: a) evolution of contact angle for a bubble on HPiS at different T_{wall}. b) evolution of equilibrium contact angle ECA for a bubble on HPiS at different T_{wall}.

The super-hydrophobic case (SHS) result is shown in Figure 31. The SHS at $T_{wall}=101°C$ multiple nucleation sites are initially activated that coalesce to create a vapor film on the surface. On SHS the bubble growing time is around 10 to 20 times higher (at the same temperature).

However, it is not possible to define the contact line or the apparent contact angles in this case, since the bubbles are formed and grow directly from a vapor film that cover all the super-hydrophobic surface.
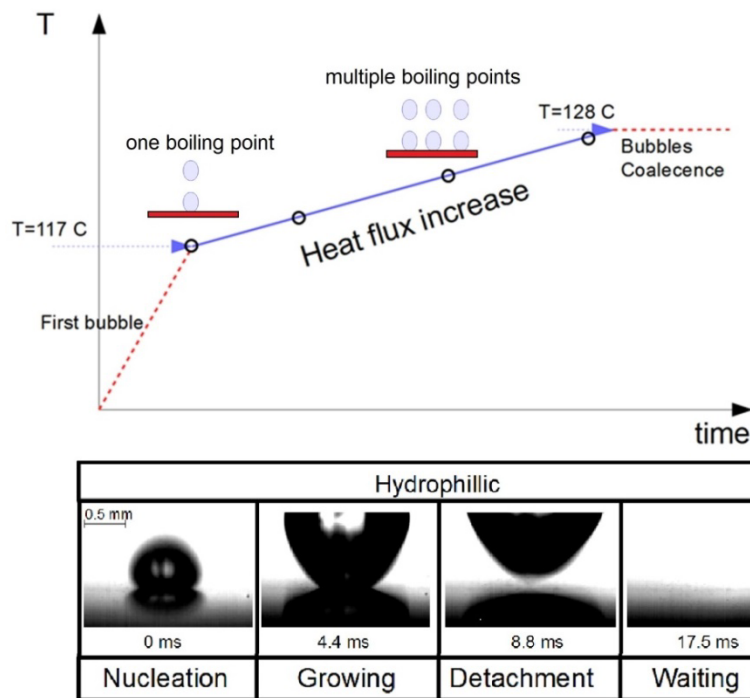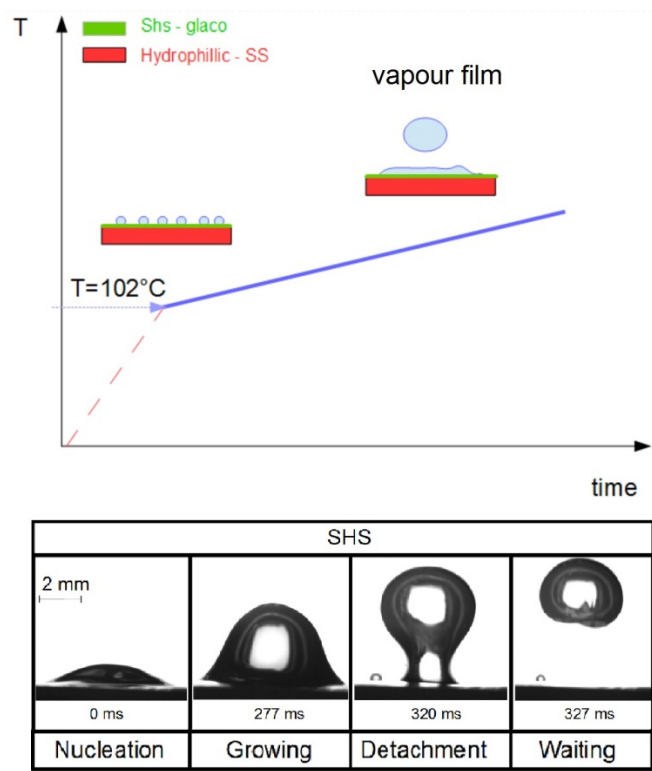

Figure 31: Super-Hydrophobic case result. The pool boiling on SHS starts on at 101°C. On the bottom there is the bubble growth and detachment process on the tested surfaces in the experiments (Four stages are identified: nucleation, growth, detachment, waiting time).

The SHS_D case(a small circle in the center of the same sample HPS is covered by the SHS coating) shows a similar beaviour (Figure 32). The nucleation sites appear only within the SHS circular part in the center of the sample (in a well-defined place), however no bubble nucleation occurs within the HPS zone as long as $T_{wall}<117°C$.
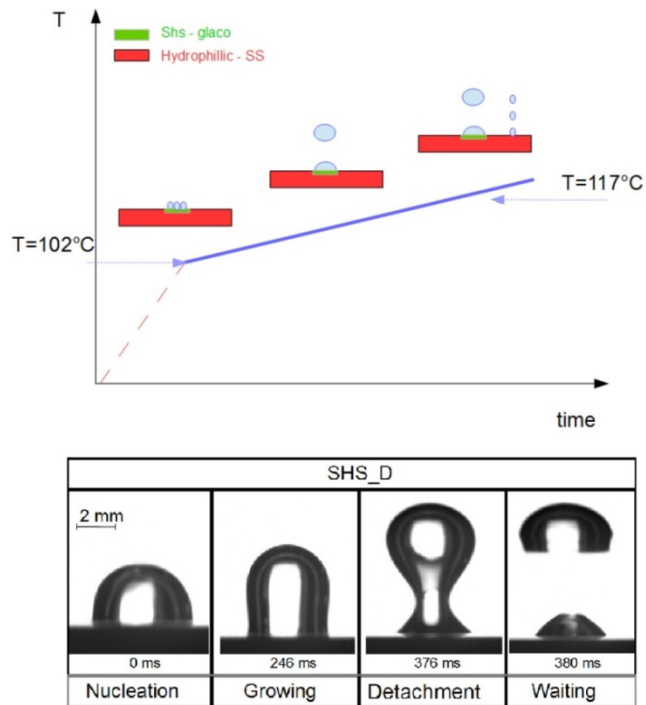
Figure 32: SHS_D case result. The pool boiling on SHS starts on at 101°C only in the SHS part. On the bottom there is the bubble growth and detachment process on the tested surfaces in the experiments (Four stages are identified: nucleation, growth, detachment, waiting time).

Even if   a sample is covered by many SHS-spot (SHS_MD in Figure 33a), the boiling starts only from SHS-spot. This clearly shows the potential of a SHS-spot to control the position of the nucleation sites.
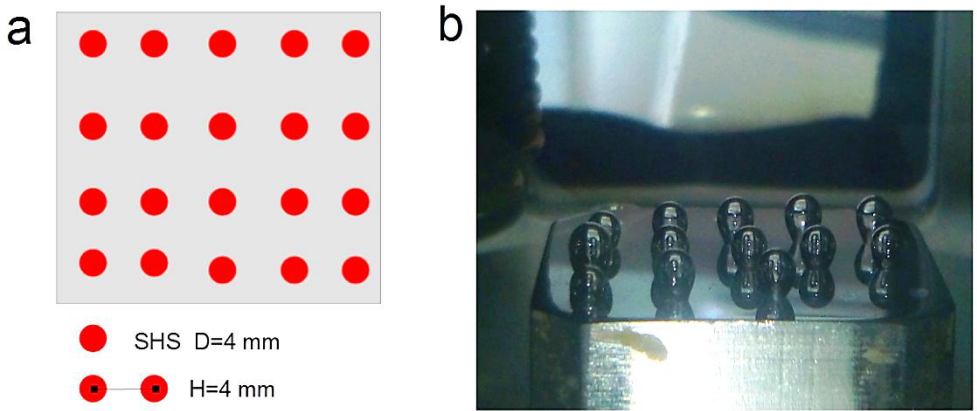
Figure 33: a) Size and distribution of the SHS-spot on the sample surface. b) visualization of the bubbles on SHS_MD

The experimental results on SHS_D and SHS_MD show that even a small zone of boiling surface is covered by Super-hydrophobic surface reduce the onset boiling temperature. However here coalescence of initial small bubbles takes place creating a film, that is bounded by the circumference of the SHS circular part.

In Figure 34 depicts the experimentally derived bubble detachment frequency (f_b) on the HPS (Figure 34a), SHS and SHS_D (Figure 34b) at different wall temperatures T_w. The frequency f_b is defined as:

$$\bar{f}_b = \frac{1}{N}\sum_{i=1}^{N}\frac{1}{t_b^i} \tag{4.1}$$

where $t_b^{\;i}$ is the time between two consecutive detachment events and N is the total number of detachment events in one video. So t_b is the sum of the growing time (for the bubble i) and the waiting time (time between the detach of the bubble i and the nucleation of the next bubble i+1). Using this definition a comparison between the HPS and the SHS cases is feasible in terms of the bubble frequency, since on the SHS cases it is not possible to identify the start of the nucleation (so it is not possible to discriminate between growing and waiting time), but only the detachment of the bubble. There is a clearly increasing of bubble detachment frequency with the heated wall temperature T_{wall}. This is primarily due to the corresponding reduction of the waiting time [76] and also due to the reduction of the detachment time. It is also characteristic that the f_b value on the HPS cases is about 10 times bigger than in the cases of the SHS and the SHS_D.
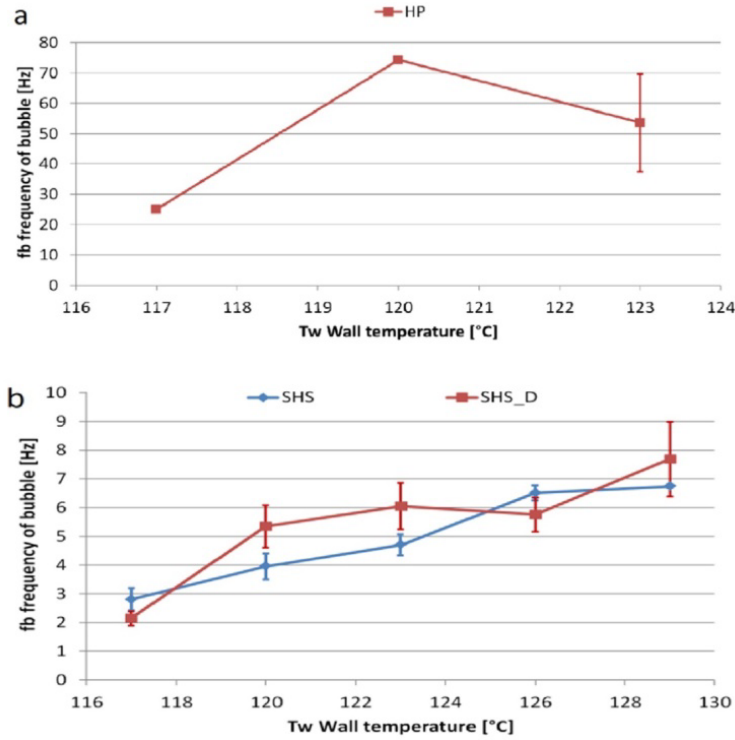
Figure 34: a) Frequency fb for the HPS in function of T_{wall} b) Frequency fb for the SHS and the SHS_D in function of T_{wall}.

The heat flux versus the superheat temperature ($\Delta T_{sh} = T_{wall} - T_{sat}$) is shown in Figure 35. The pool boiling starts earlier on SHS, however the HTC on HPiS is higher if $T > T_{ONB}$ of HPiS. Indeed at this temperature condition the SHS surface is already in film boiling regime [42], with a resulting lower HTC than the HPiS (that it is still in pool boiling regime).
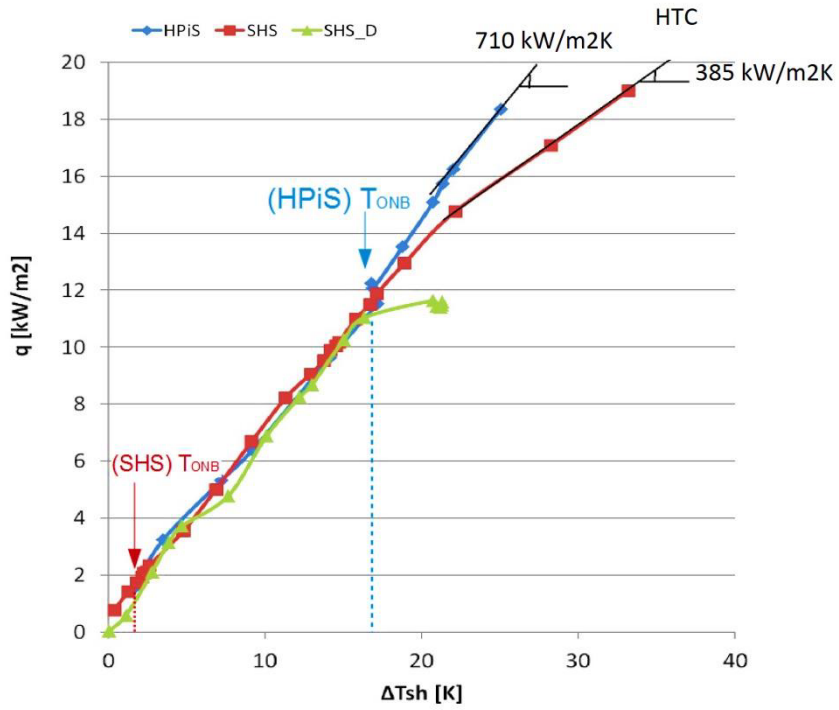
Figure 35: Heat flux versus ΔT_{sh} for HPiS, SHS and SHS_D cases. The T_{ONB} and HTC at high temperature is depicted for case HPiS and SHS.

It is possible to summarize the effect of super-hydrophobic surface as follow:

> ➢ The SHS is able to reduce considerably the T_{ONB} compare to the hydrophilic surface.

> ➢ The SHS create a vapor film on the surface (film boiling), this prevents the using of a surface completely SHS in a pool boiling regime.

According with this consideration, in the next paragraph an experiment using a small (100µm) single cavity will be use to clarify the effect of SHS in the case the SHS area is micrometric.

4.3 Single cavity experiment

In this paragraph is presented a pool boiling experiment of a sample with an artificial cavity (Figure 36). The tested sample is a stainless steel (AISI 316). The surface tested is primarily lapping to obtain a Ra<0.1µm. Then using an Electrical discharge machining (EDM) a micrometric hole (diameter of 100 µm and depth of 50 µm) is created in the center of the sample. In this case all the surface is hydrophilic (called HPi_cavity). After the pool boiling test of this sample, only the internal micro-hole is covered by SHS (Glaco Mirror Coat Zero©). This sample is called SHS_cavity.
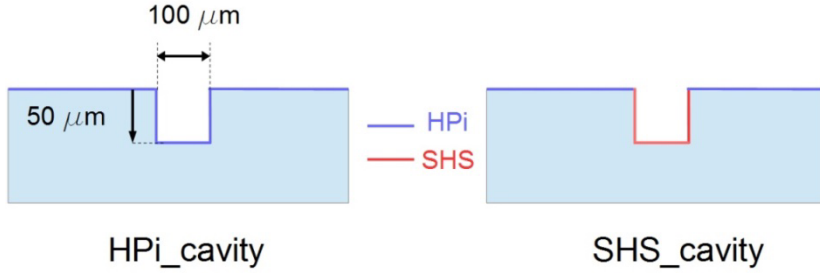
Figure 36: Geometry of sample with microcavity. The microcavity
diameter is 100µm and the depth is 50 µm. Two samples

Figure 37 shows the images from high speed camera on Hpi_cavity and SHS_cavity. The experiment is done at T_{wall}=117°C. These images show that the bubble evolution is similar for HPi_cavity and SHS_cavity, because in the both cases the bubble growth up on the same hydrophilic substrate. However the T_{ONB} for the HPi_cavity is 114°C, higher than the T_{ONB} for SHS_cavity (104°C), because T_{ONB} is function of wettability in the nucleation zone (the cavity for these experiments).
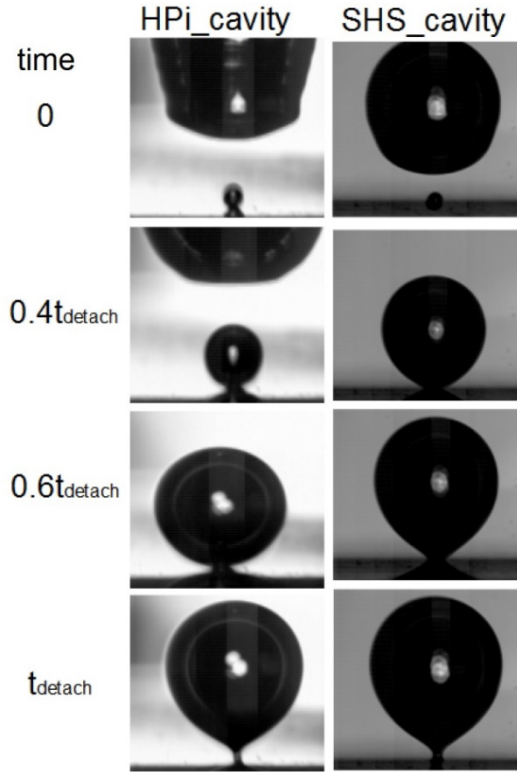
Figure 37: Evolution of a bubble in a pool boiling condition for HPi_cavity and SHS_cavity.

In the Figure 38 The heat flux versus the superheat temperature ($\Delta T_{sh} = T_{wall} - T_{sat}$) is shown. The heat transfer coefficient is the same for both case, because HTC is depend on bubble growth evolution (similar for HPi_cavity and SHS_cavity). However the SHS_cavity provides a low T_{ONB} also in the presence of a cross flow on the surface, as demonstrated in the next paragraph.
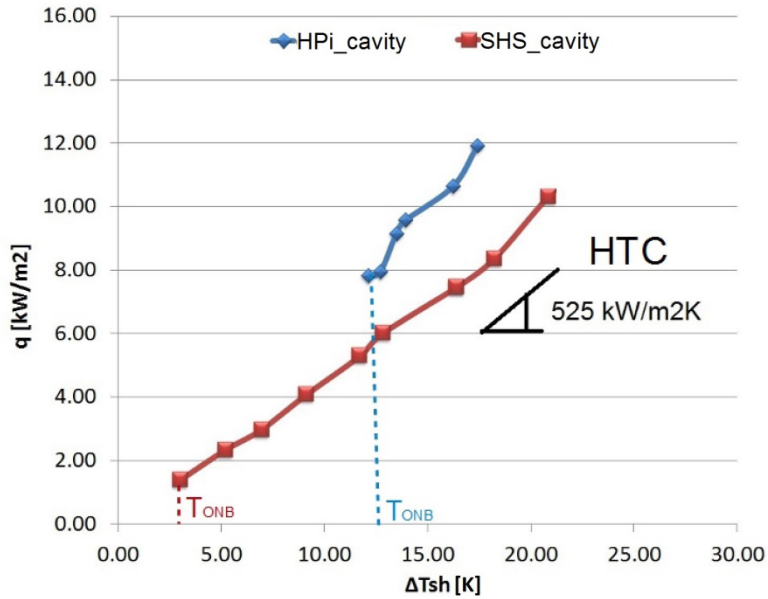
Figure 38: Heat flux versus ΔT_{sh} for HPi_cavity and SHS_cavity. The T_{ONB} and HTC at high temperature is depicted.

4.4 Cross flow boiling

The apparatus presented in paragraph 4.1 is modified in order to create a cross flow close to the boiling surface. In Figure 39 is shown the new

configuration of the pool boiling apparatus. A channel (circular tube with internal diameter of 8 mm) is been in contact with the sample surface. The flow is create by an external circuit. A pump (LIQUIPORT ® NF) is used to fix the flow rate in the circuit. Between the pump and the channel a dumper (FPD 06 KNF®) reduces pulsations downstream of the pump, and a thermocouple measures the temperature of the liquid in the circuit, to control the heat loss of the external circuit. Finally two valves (inlet and outlet) enable to separate the circuit from the chamber.
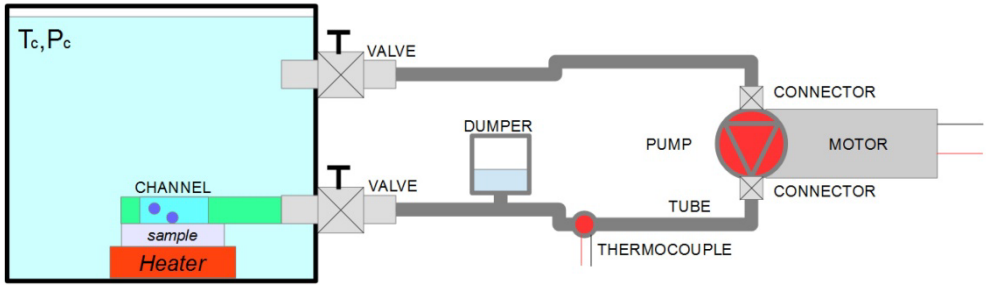
Figure 39: Modification of the chamber for cross flow boiling experiment.

The protocol used for each boiling experiment is performed is shown in Figure 40.

I. the vacuum is pulled using a vacuum pump inside the chamber and the circuit, until a pressure of about 60 millibars, in order to remove a maximum of air and adsorbed gases (t_a).

II. A degases water starts to fill the chamber (t_b) until completely fills the box.

III. After the filling of the chamber, the internal heater (Int heater) is then turned on to heat up the water temperature. When the water temperature reach about 80°C (t_{bf}) the circulation pump is switched on, and a cross flow is start on the sample surface.

IV. At t_c the temperature of the liquid is close to the saturation temperature. To keep the pressure (and thus the temperature) at the desired saturation value (point t_c), an external air cooling system of the top wall controls the steam to condense on the roof the chamber and avoids the variation of the pressure.

V. When saturation conditions in a chamber are stable, the acquisition of data starts (using a data acquisition/switch unit). The values of temperature (T_w, T_{ch}) pressure (P_{ch}) and heat flux (W/m2) are recorded during the experiment. Heater sample is switched on and the power given to the surface is incrementally increased to work in stationary conditions. A high speed camera record the pool boiling process. Reached the desire wall

temperature (t_d) the flow rate is changed by the pump. Four different flow rates are analyzed (0.2-0.5-1-1.3 l/min) for each T_w.
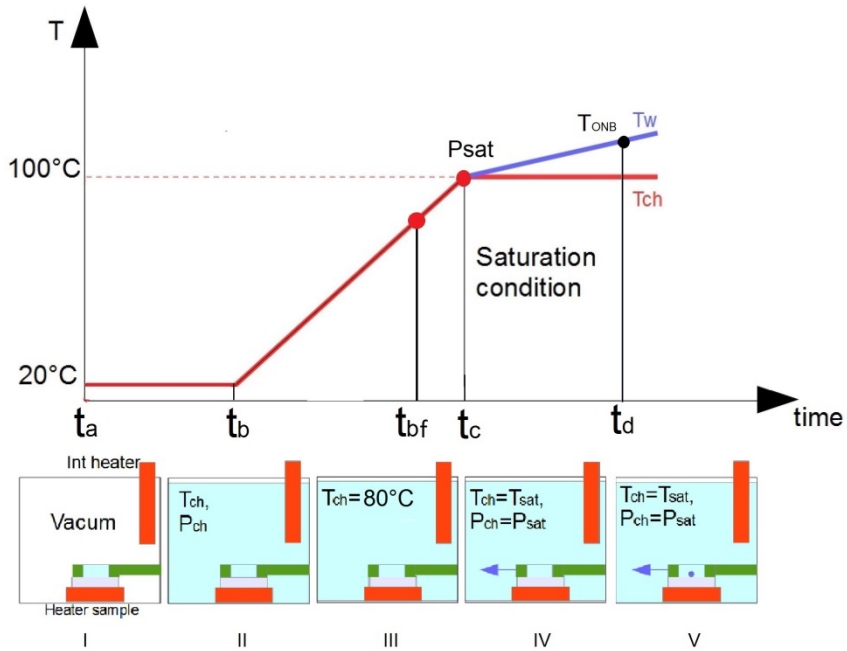
Figure 40: Cross flow boiling experimental procedure.

In a cross flow pool boiling, the total heat flux from the wall is the sum of three terms [77]:

$$q''_{NB} = q''_{conv} + q''_{eva} + q''_q \qquad (4.2)$$

Where q''_{conv} is the single-phase convective heat flux, due to the cross flow, q''_{eva} is the heat flux associate with phase change (boiling) and q''_q is the so-called quenching heat flux, which is transferred to the liquid phase during the waiting ime (The heat transfer from the wall in the vicinity of a nucleation site occurs during the bubble growth time, boiling, and the waiting time).

In Figure 41 is shown the outcomes resulting from the cross flow boiling experiment. Two outcomes are observed:

> **Static bubble:** bubble is generate but it sticks on the surface. The ΔT_{sh} is not enough to sustain the growing and detachment of the bubble.

> **Pool Boiling:** If the ΔT_{sh} is enough high, the bubble is able to growth up and detach from the surface. Figure 42 shows the evolution of a bubble in boiling pool cross flow regime. The temperature of the wall is $T_w \geq 119°C$, for 4 different flow rates are analyzed (0.2-0.5-1-1.3 l/min).
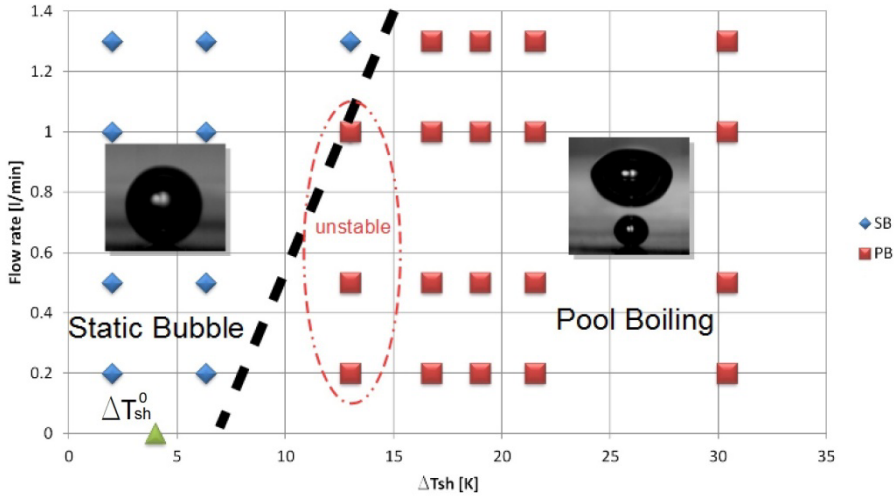
Figure 41: Outcomes of the cross flow boiling experiment, for a flow rate between 0.2-1.4 l/min and a ΔT_{sh} from 2 K to 30.4 K. ΔT_{sh}^0 indicate the superheat temperature for the onset of boiling if the flow rate is 0. At ΔT_{sh}=13 K there is the transition between two outcomes.

The ΔT_{ONB} (when the first pool boiling regime appears) in this test is about 10-13°C. At ΔT_{sh} =13°C the pool boiling regime appear for a flow rate between 0.2 to 1 l/min. However the pool boiling is unstable. The waiting time between one bubble detachment and the new nucleation is on the order of few second. Then at ΔT_{sh} =17°C for all the flow rate values (0.2-1.3 l/min) a clear pool boiling regime appears. This value is higher than Tonb in the absence of the cross flow (T_{onb}=105°C). Due to

87

the cooling effect of the cross flow (q''_{conv}), it is required a higher temperature of the surface to have the boiling nucleation. Furthermore the heat loss due to the external circuit reduce the temperature of the water in contact with the sample surface. The measure the circuit temperature (by thermocouple in Figure 39) shows that the temperature of the flow is around 97°C-96°C (sub cooling regime).
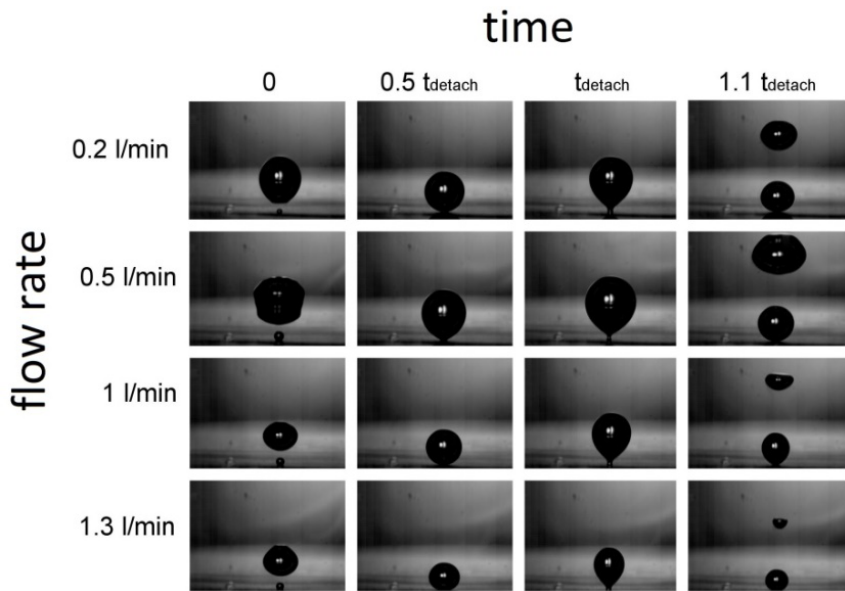
Figure 42: Evolution of a bubble in boiling pool cross flow regime. The temperature of the wall is T_w=119°C. Four different flow rates are analyzed (0.2-0.5-1-1.3 l/min) and the results are shown in function of detach time of each bubble (t_{detach}).

The values of the detach time (t_{detach}) are shown in Figure 43. The detach time is evaluated for for 5 different temperature (from 117°C to 130°C) and 4 flow rates (from 0.2 to 1.3 l/min). However there is a clear decreasing of the detach time if the temperature increases (according with [78]).
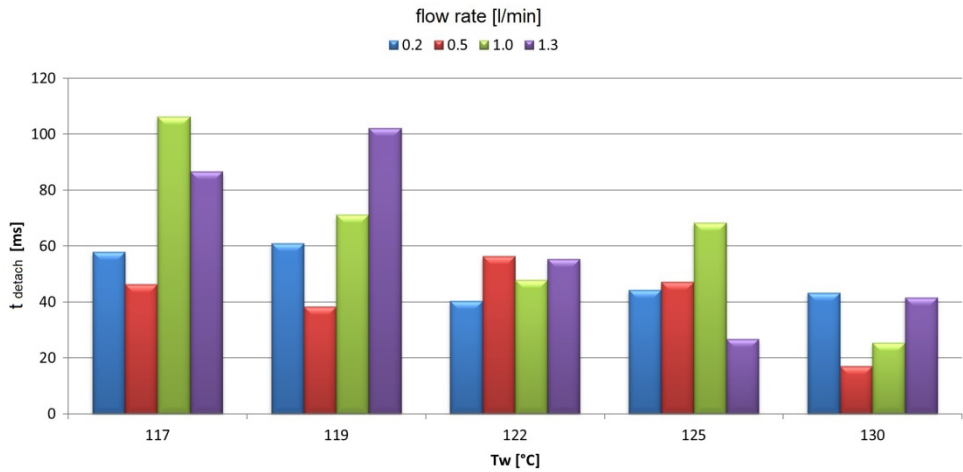
Figure 43: evaluation of detach time (t_{detach}) for 5 different temperature (from 117°C to 130°C) and 4 flow rates (from 0.2 to 1.3 l/min).

Chapter5

5 Pool Boiling Simulation

5.1 HPiS Simulation method

Simulation results of an experimental case (pool boiling on HPiS at $T_w=117°C$) is presented in this paragraph. The aim of the simulation is to check the ability to capture the apparent contact angle variation with time. For this purpose, two contact angle model are used:

- **Static contact angle model:** fixed value of the contact angle on the wall, equal to the equilibrium contact angle.

- **Dynamic contact angle model:** numerical treatment for the triple-line contact angle that take into account the advancing and receding value of the contact angle at equilibrium. The contact angle on the wall is change from advancing to receding depending on velocity direction of the contact line.

The numerically predicted results from both treatments are compared with the corresponding experimental data.

Since the process of bubble growth and detachment in the proposed experiment can be considered to be axisymmetric, an axisymmetric computational domain was constructed for its numerical reproduction. A wedge type computational geometry was constructed (Figure 44), representing a 5° section of the corresponding 3D domain in the considered physical problem. A non-uniform structured computational mesh with local refinement was used consisting of 400,000 hexahedral cells. A minimum cell size of 6μm and a maximum cell size of 50μm were selected in the bottom left and top right corners of the computational domain respectively, in order for the solution to be mesh-independent. The overall domain size in the XY plane was 10 mm x 16 mm. These dimensions were indicated from initial, trial simulations that were conducted in order to determine the minimum distances between the axis of symmetry and the side wall boundary (domain width) as well as between the bottom wall and the outlet (domain height), in order to avoid any influence of these boundaries in the computed bubble growth and detachment process.
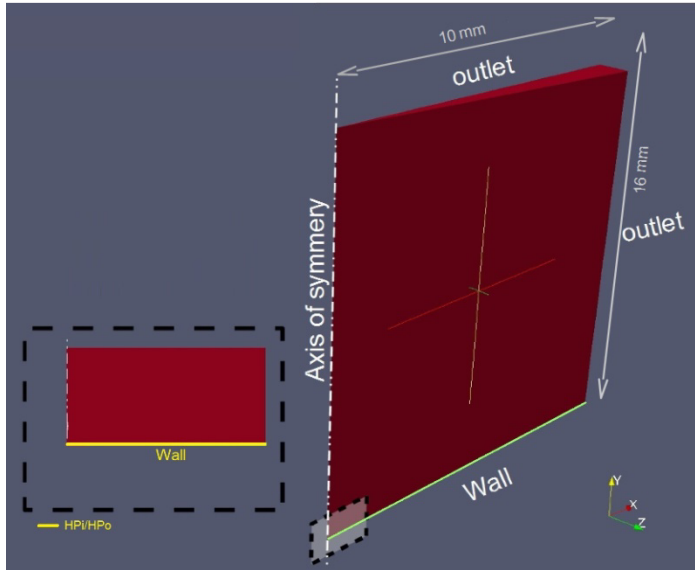
Figure 44: Domain for numerical simulation.

At the solid wall, a no-slip velocity boundary condition was used with a fixed flux pressure boundary condition for the pressure values. At the lower wall, either a constant contact angle of $\theta_{eq} = 58^o$, or a dynamic contact angle with $\theta_{adv} = 74^o$, $\theta_{rec} = 43^o$ and $\theta_{eq} = 58^o$ is imposed for the volume fraction field (according with HPiS value in Table 3). For the sidewall, a zero gradient boundary condition was used for the volume fraction values. As for the temperature field, a constant temperature of $T_w = 117°C$ (in accordance to the selected experimental run) was imposed in the bottom wall and a constant temperature of $T = 100°C$ was used for the sidewall (saturation temperature). At this point it should be mentioned that for the simulation a constant temperature boundary condition was

92

used for the heated wall, while in the experiments the proposed temperature might not remain totally constant during the bubbling process. At the outlet, a fixed-valued pressure boundary condition and a zero-gradient boundary condition for the volume fraction were used, while for the velocity values a special (combined) type of boundary condition was used that applies a zero gradient when the fluid mixture exits the computational domain and a fixed value condition to the tangential velocity component, in cases that fluid enters the domain. Finally, a constant value boundary condition for the temperature field, equal to the saturation value, was also prescribed at the outlet boundary. The fluid properties are kept constant.

5.2 HPiS Simulation method

Simulation results can be found [75]. The numerically predicted spatial and temporal evolution of the interface between the liquid and vapor phases for the case of the HPS (T_{wall}=117°C) is illustrated in Figure 45 using the constant contact angle treatment (left) as well as the dynamic contact angle treatment (center). On the right in Figure 45 the equivalent experimental case is shown. As it can be observed, in both cases the bubble detachment time is similar, t_{det}=12.8 ms, which is quite close to the experimentally estimated time of detachment (8.7 ms). However, the equivalent bubble detachment diameter in the case of the dynamic contact angle treatment (D_{eq}=2.62 mm) is much more closer to the experimentally

calculated value (D_{eq}=2.50 mm) as well as to the theoretical correlation of Fritz [79] (D_{eq}=2.34 mm) than in the case of the constant contact angle treatment (D_{eq}=2.04 mm).
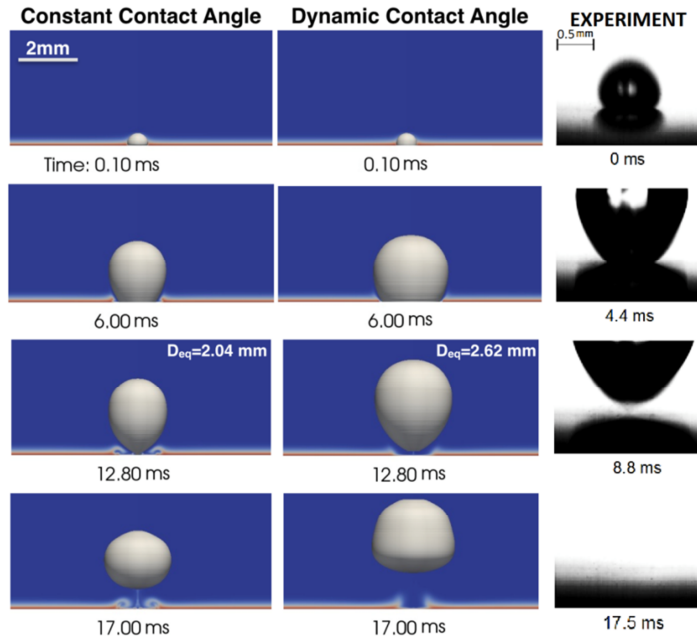
Figure 45: Sequence of the bubble growth and detachment process for the HPS from the numerical reproduction of the same experimental run, with a constant contact angle (left) and a dynamic contact angle treatment (center). The same experimental case is shown on the right[75].

A comparison of the dynamic, apparent contact angles between the experiment (red line) as well as the numerical simulations with the constant contact angle treatment (green line) and the dynamic contact angle treatments (blue line), is made in Figure 46, for the case of T_{wall}=117°C. The apparent contact angle is evaluated in the simulation using the same image processor, applied to the images from experimental tests.

As it can be observed the dynamic contact angle treatment is again more close to the experimental curve, especially at the last stage of the bubble growth, before its detachment from the heated plate. Therefore, it is evident that the dynamic contact angle treatment gives better results regarding both the bubble detachment characteristics as well as the apparent contact angle revolution with time, in comparison to the corresponding experimental data.
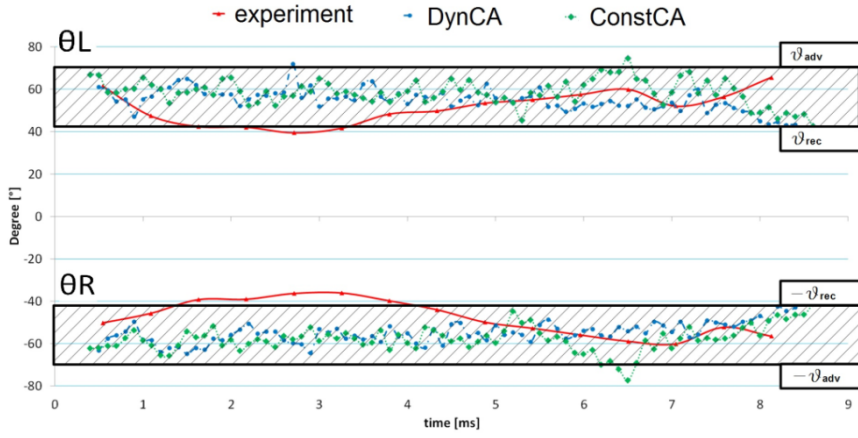
Figure 46: a) Apparent dynamic contact angles θ_R and θ_L for HPS surface. Comparison of the experimental measurements with the corresponding numerical predictions for both the constant as well as the dynamic contact angle treatments[75].

Chapter6

6 SH polymeric coating

6.1 Coating preparation and characterization

It is known that crystallized polypropylene particles show superhydrophobic properties (EP patent number *2726518 B1*). Crystallized polypropylene (PP) particles deposited onto a substrate confer superhydrophobic propertxies to the substrate surface. Superhydrophobic polypropylene particles may be used in the preparation of construction materials, insulation materials, or in coatings. The preparation of the proposed SH polymeric coating can be found in the GB patent *1610678.3*. It is prepared from two SH polymeric compositions, synthetized in order to obtain different sizes of crystalline PP grains. The preparation of the one coating composition (OPS) containing 30 wt% of crystalline PP polymer mixed in a dissolved epoxy resin. This solution creates a PP/epoxy suspension. The OPS preparation and characteristics are described in GB patent *1622380.2*. Two different OPS compositions

are prepared, to obtain two different size PP grain distribution (called OPS_BIG and OPS_SB). A homogeneous and heterogeneous (biphilic) wettability can be obtain from these OPS solution (Table 5):

➢ **Homogeneously covered surface (named FILM_OPS)**

A 1 ml of the OPS_SB is applied by air brushing technique using a spray gun. The OPS is sprayed at an air pressure of 20 psi onto a vertical stainless steel sample of 32 x 32 mm. The spray nozzle was held at a distance of approx. 50 cm from the surface to be coated. Spraying is performed by moving the spray gun in forth and back movements, more particularly up and down in this instance.
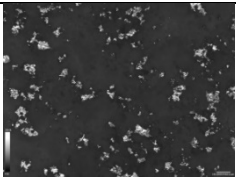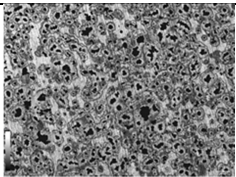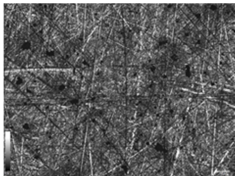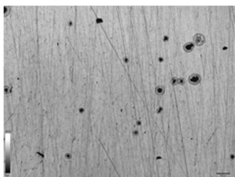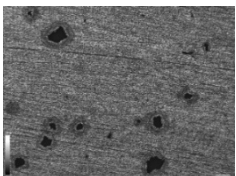
The coated surface obtained here above is then coated with a further layer of epoxy resin. A 1 ml of the epoxy solution is sprayed onto the super-hydrophobic coating in the same way. The coated surface is then allowed to dry again. The above described spraying processes are repeated two further times in order to alternate one pot solution and epoxy resin and allowing the solvent to evaporate between sprays. The resulting coating is treated in an oven at 60°C during 16 hours and at 120°C for 2 h. The coated surface showed a homogenous super-hydrophobicity characteristics on all the surface (equilibrium contact angle of 135°).

➢ **Heterogeneous covered surface (named DOT_OPS)**

The spraying method used for FILM_OPS is used to obtain biphilic characteristics, where SHS points are dispersed on top of the hydrophilic surface. For this purpose, the distance of the spray nozzle from the surface to be coated and the aliquot are varied as well as described in Table 5. In this way, it is possible to control coarsely the distance between the SH points created by the OPS as well as the percentage of the stainless steel surface that will be SH. After spraying, the resulting coating is treated in an oven at 60°C during 16 hours. The prepared samples are (see Table 5):

➢ *FILM_OPS:* Homogeneous covered surface using OPS_BIG

➢ *DOT_OPS_BIG_HD*: SHS points dispersed on the hydrophilic surface with high density, using the OPS_BIG

➢ *DOT_OPS_BIG_LD*: SHS points dispersed on the hydrophilic surface with low density, using the OPS_BIG

➢ *DOT_OPS_BIG_ULD*: SHS points dispersed on the hydrophilic surface with ultra-low density, using the OPS_BIG

➢ *DOT_OPS_SB_LD*: SHS points dispersed on the hydrophilic surface with low density, using the OPS_SB

Table 5: Characteristics of the heterogeneous coated surface.

Samples name	Aliquot [ml]	OPS	Spray distance (cm)	Microstructural aspect [2.55 mm x 1.91 mm]
FILM_OPS	1	BIG	50	
DOT_OPS_BIG_HD	0.5	BIG	50	
DOT-OPS_BIG_LD	0.25	BIG	50	
DOT_OPS_BIG_ULD	0.25	BIG	120	
DOT_OPS_SB_LD	0.25	SB	120	

After deposition of the coating, it is possible to characterize the heterogeneous surfaces named DOT_OPS by these parameters:

- $\overline{Gsize}$: Average size of the grain on the surface

- $\overline{minDist}$: Minimum average distance of the grains.

- *%SHS:* Percent of surface covered by SHS grains.

These values are obtained by 5 real images (1mm x 2.5 mm, confocal microscope Sensofar©) for each DOT_OPS surface. A Matlab script is created to evaluate size and minimum distance of the grains. Figure 47 shows an explicative example (*DOT_OPS_BIG_HD*) for the image processing that is carried out in all the coated. The size of the grains and the minimum distance between the grains assume a distribution of values. The average values of the minimum distance between the grains $\overline{minDist}$ can be modify by sparying process parameters, the average value of the size distribution $\overline{Gsize}$ is modified during the OPS preparation (the size PP grain). The percent of the surface covered by SH grains are depending on these two values: high value of **%SHS** can be obtained for Low $\overline{Gsize}$ or high $\overline{minDist}$. The upper limit of **%SHS** (100%) is obtained by FILM_OPS (see Table 6). The value of Ra[3] for the

---

[3] Ra is the arithmetic average of the absolute values of the profile height deviations from the mean line, recorded within the evaluation length. Simply put, Ra is the average of a set of individual measurements of a surfaces peaks and valleys.

tested surface is evaluated by confocal microscope (area of measurement is 0.6 mm x 0.47 mm, confocal microscope Sensofar©).

Table 6: $\overline{Gsize}$, $\overline{minDist}$ and **%SHS** for the tested surfaces.

Sample name	$\overline{minDist}$ [µm]	$\overline{Gsize}$ [µm]	%SHS	Ra [µm]
FILM_OPS	0	-	100%	42.24
DOT_OPS_BIG_HD	62	29	9%	0.7
DOT_OPS_BIG_LD	130	31	2%	0.6
DOT_OPS_BIG_ULD	255	37	1%	0.05
DOT_OPS_SB_LD	279	65	2%	0.17
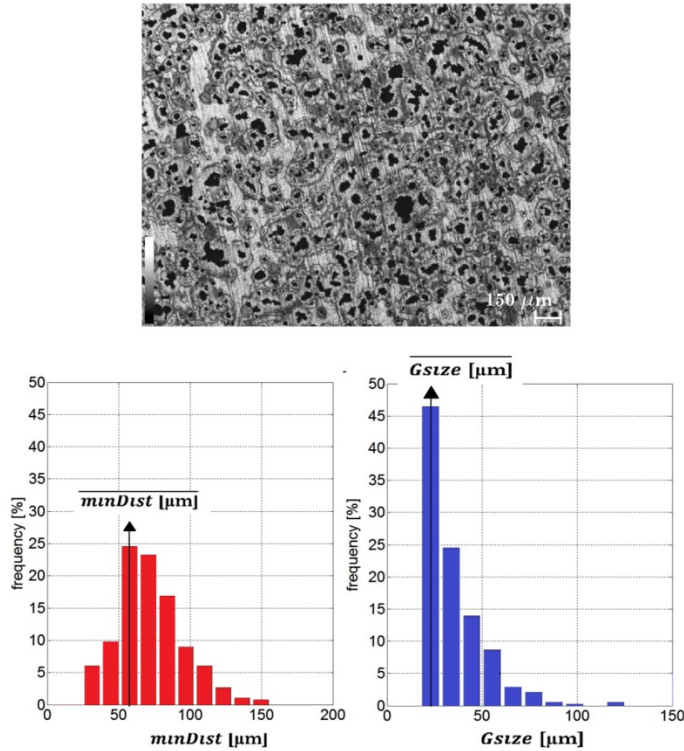
Figure 47: Image processing to evaluate the grain size and distribution on the *DOT_OPS_BIG_HD*.

6.2 Pool boiling test

The test procedure for the pool boiling test on the new coating is shown in Figure 48. As in the previous pool boiling tests, first the temperature of the complete system (chamber and sample) is increased up to the saturation temperature of the pure water at atmospheric pressure (100°C).

103

Then the saturation conditions of the pure water in the chamber ($T_{ch}=100°C$ and $P_{ch}=101.3$ kPa) are maintained with the PID system after point b in Figure 48. Thereafter, only the temperature of the sample is gradually increased. This first increasing of the sample temperature is called 1st ramp (b-c) and it was systematically performed as a blank in order to remove all the peculiarities of the initial conditions in the setup cell and on the surface of the sample. After reaching a sample temperature of 130°C, the sample temperature is decreased (c-d) back to 100°C (saturation conditions of pure water). Finally, the sample temperature is increasing again (points d-e). This last increasing is called 2nd ramp and it is performed to characterize the pool boiling performance of the samples. The first ramp is used to obtain the same initial condition on the sample surface, in term of gas/vapour concentration. The T_{onb} during the first ramp could be influenced by different concentration of the gas/vapour for different tested samples [80]. Therefore the ebullition on the coated samples during the first ramp ensures to have enough gas/vapour concentration in all the surfaces of the surface samples on the second ramp, not dependent on the apparatus setup.

.
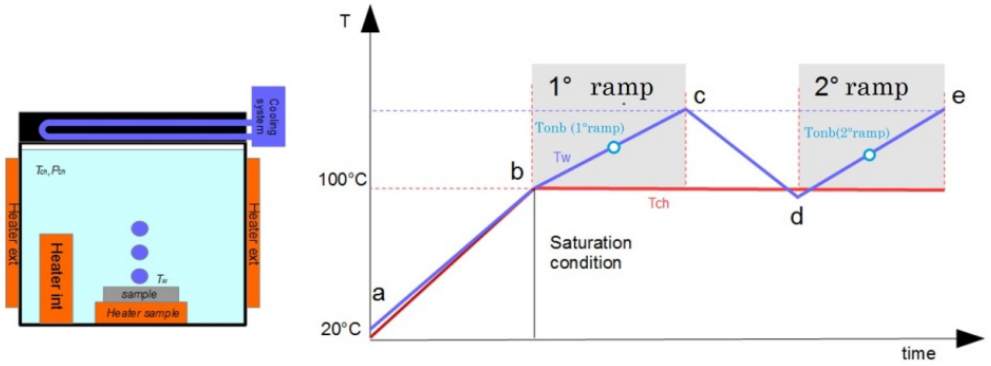
Figure 48: Schematic representation of the test set up and procedure for
SH polymeric coating.

In Figure 49 is shown the T_{ONB} obtained for the different tested surfaces.
The homogeneous values of T_{ONB} (2°C of max difference) during the
second ramp for biphilic surface (DOT_OPS) and the invention coating
(FILM_OPS) that indicate the proper operating of the SH grains on T_{ONB}
reduction.
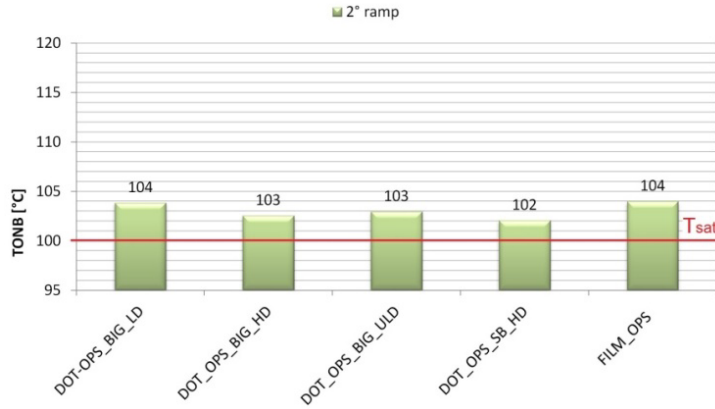
Figure 49: T_{ONB} during 2nd ramp for the tested surfaces.

Figure 50 gives the heat flux curve versus the wall temperature for the different tested surfaces. As can be seen, the sample named DOT_OPS_BIG_LD has the best performance. The FILM_OPS has good heat flux for low wall temperature, but the formation of the film induces a significant reduction of heat transfer coefficient at higher temperature (decreasing of the FILM_OPS curve start at 118°C). This transition to film boiling is not present on DOT_OPS cases (for the tested T_{wall}).
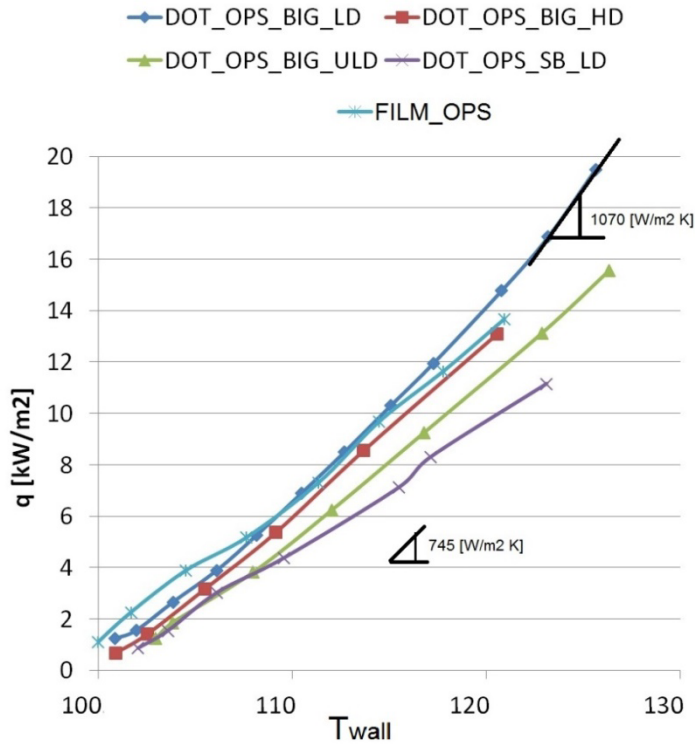
Figure 50: Heat flux versus wall temperature during 2° ramp for the tested surfaces.

Concerning the critical heat flux parameter (CHT), this value cannot be measured with the apparatus of LPSI laboratory, because the maximum wall temperature that can be reached by the apparatus is 140°C. On the other hand, the SHS coating showed in Chapter 3 reaches the CHT condition (forming a vapor film on the surface) at very low temperature

107

(105°C). On the contrary the DOT_OPS coatings do not show any film boiling condition up to 135°C.

6.3 Improvement of thermal and mechanical resistance

This paragraph gives two possible solutions to improve the thermal and mechanical resistance of the coatings in order to maintain the wettability characteristics in pool boiling conditions. Both of these techniques are described in more detail in GB patent *1622380.2*.

> ➤ **First method for the development of a durable heterogeneous coating**

A thin film of hydrophilic epoxy is deposited on the stainless steel (a2 in Figure 51) substrate by the spin-coating of 0.5 ml of solution at 3000 rpm during 2 min. On the second step the SH grains were placed on the surface by the spraying technique previously explained for heterogeneous covered surfaces (a3 in Figure 51). The resulting coating were allowed to cure in an oven at 60°C during 16 hours. It is expected that the SH grains will be partially immerse and surrounded by the epoxy glue preventing the detach from the surface, and partially outside the epoxy film. The epoxy film prevents the detachment of the grain from the surface. The

Figure 51 shows a schematic representation of the procedure (first method on the left). The sample prepared by this method is named *DOT_OPS_BIG_HD_EPOX_HPi*. The Ra is 2.28 μm (area of measurement is 0.6 mm x 0.47 mm, confocal microscope Sensofar©).

> **Second method for the development of a durable heterogeneous coating**

A first layer of hydrophilic epoxy is deposited on the stainless steel substrate by the spraying technique as in the previous method (a1 in Figure 51). On a second step, a homogeneous layer of glass microspheres (Diameter≈1000 micron) are located above this first layer in order to cover all the surface under study (b1 in Figure 51). On the third step a homogenous film of the SH polymeric composition (OPS_BIG) was applied also by spraying (b2 in Figure 51). The resulted coating was allowed to cure in an oven at 60°C during 16 hours. As a final step, the top layer of SH polymeric coating was removed from the glass (b3 in Figure 51). The sample prepared by this method is named *MS_1000_EPOX_HPi_OPS_B_FILM*.

For comparative purposes of the boiling behavior a stainless steel surface coated by a first layer of Hpi epoxy and covered with the microsphere

was also prepared (b1 in Figure 51), this sample is named *MS_1000_EPOX_HPi.*
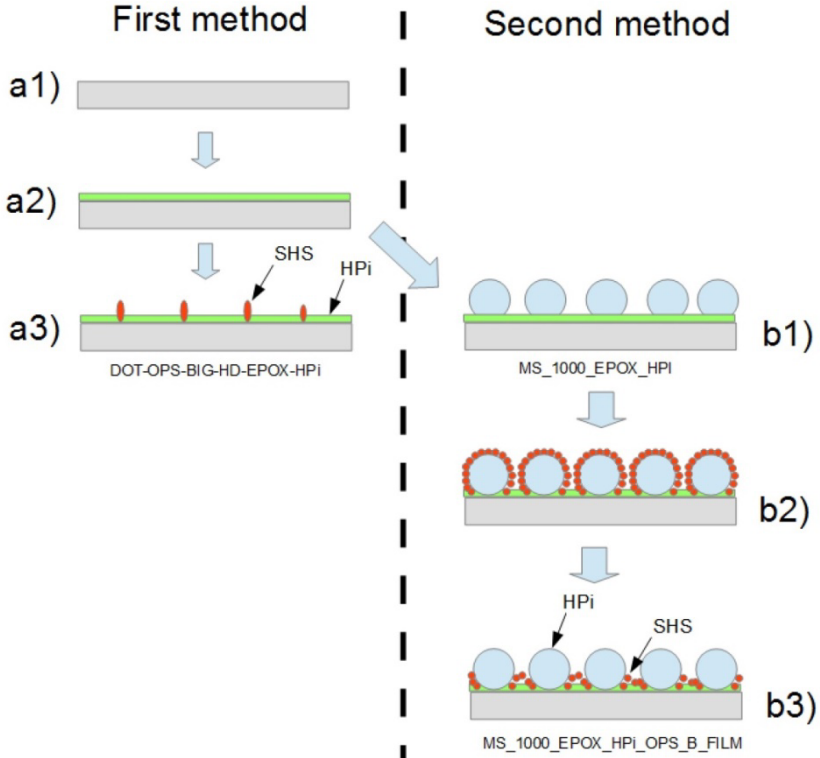
Figure 51: Schematic representation of the first method (on the left) and second method (on the right) to improve mechanical and thermal resistance. 3 samples are resulting from these methods (*DOT_OPS_BIG_HD_EPOX_HPi, MS_1000_EPOX_HPi_OPS_B_FILM and MS_1000_EPOX_HPi)*

The resulting of T_{ONB} are shown in Figure 52:

> ➤ The presence of the microspheres seems to increase the temperature to activate the boiling (T_{ONB}). Using an insulating material for the microsphere (glass) can effectively produce an increase of the superheat temperature to generate pool boiling (*MS_1000_EPOX_HPI*).

> ➤ However, with the OPS coating (*MS_1000_EPOX_HPi_OPS_B_FILM*) the T_{ONB} is lower.

> ➤ Finally, the layer of hydrophilic epoxy does not reduce the effect of super hydrophobicity (*DOT_OPS_BIG_HD_EPOX_HPi*). The higher reduction of T_{ONB} in this case, compared with the experiment without hydrophilic epoxy, can be explained with the higher %SHS (approximately 17% of the surface is covered by grains).
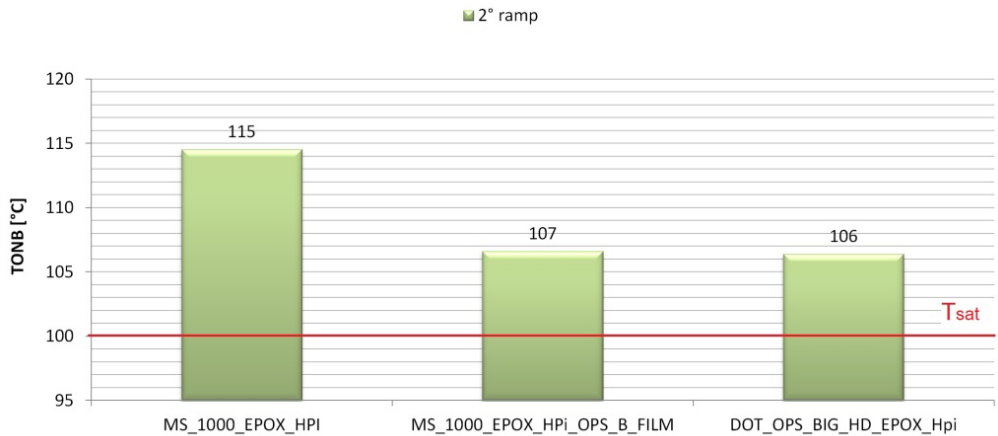
Figure 52: T_{ONB} for the tested surfaces during 2°ramp in pool boiling test

6.4 Thermal cycle test

In the real applications an hypothetic coating for heat transfer application should maintain its wettabilities properties even after a reasonable number of startup of the apparatus. This paragraph describes the procedure for a thermal cycle test to simulate a real application in which the coating is subject to a cycling variation of the temperature (between saturate and no-saturate condition) as it is expected in a real case. Two samples (already presented) are tested:

➢ *DOT_OPS_BIG_HD_EPOX_Hpi*

➢ *FILM_OPS*

The goal of the thermal cycle test is to check the adhesion resistance of the grains through the thin film of hydrophilic epoxy and the maintaining of the super hydrophobicity of the coating.

Figure 53 shows the apparatus used for the thermal cycle experiment: the two samples are immersed in pure water in a glass chamber. The temperature of the glass chamber is varied by an external recirculation of oil fluid. The oil is sourced alternatively (using a timed valve) from two different baths (Julabo©). The temperature of each bath is set in order to generate the desire temperature variation shown at the top-left of Figure 53. A thermal cycle starts with the water at saturation condition (T1=100°C) at ambient pressure. This condition is maintained for 15 min and thereafter the water temperature (T_{ch}) is decreased to 80°C (no saturation condition) and maintained for 25 min. Thereafter a new cycle is started with T_{ch} again at saturation conditions (T_{ch}=100°C). Each cycle lasted 40 minutes, and the cycles were repeated respectively 156 and 506 times. A water reservoir is connected with the bottom of the water chamber in order to compensate for loss by evaporation. The water temperature (T_{ch}) is recorded during the test using a K-thermocouple inside the water chamber.

113
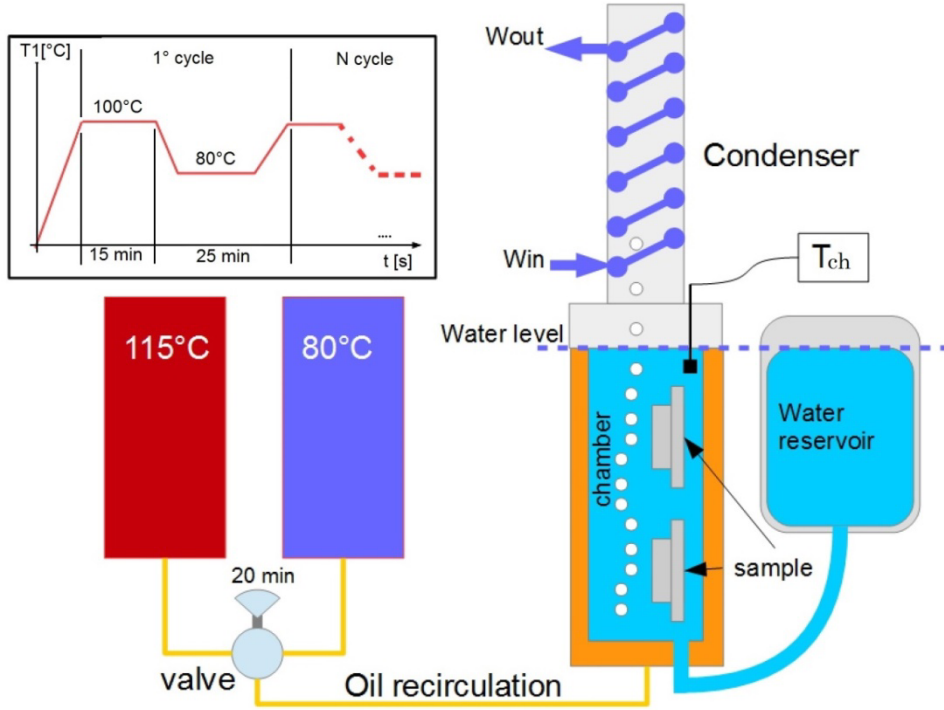
Figure 53: Durability Test Apparatus

The pool boiling experimental test, as describe in chapter 7.2, performed in order to evaluate the T_{onb} after 156 and 506 cycles. of the equilibrium static contact angle (using a Krüss© DSA 100), was carried out on *FILM_OPS* after 0-159-506 cycles. The T_{ONB} values for both samples (*DOT_OPS_BIG_HD_EPOX_Hpi* and *FILM_OPS*) are presented in Figure 54. No significant variation of T_{ONB} value has been noticed.
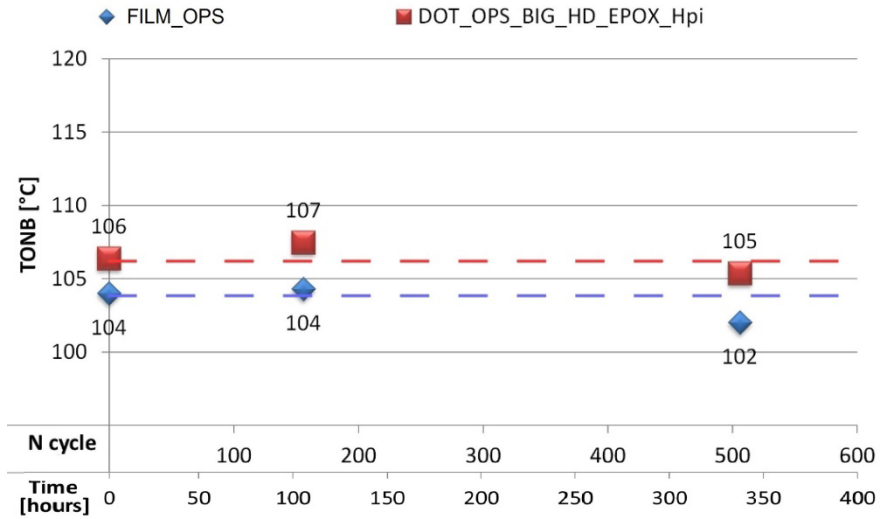
Figure 54: T_{ONB} for the tested surfaces during 2°ramp in pool boiling test.

In addition, contact angle measurement (using a Krüss DSA 100) is done on FILM_OPS after 0-159-506 cycles test. The DOT_OPS_BIG_HD_EPOX_HPi has a biphilic structure, and it is not possible to measure the contact angle with a sessile drop of few millimeters. Figure 55 shows that the equilibrium contact angle remains approximately the same, and there is no significant variation of equilibrium contact angle.
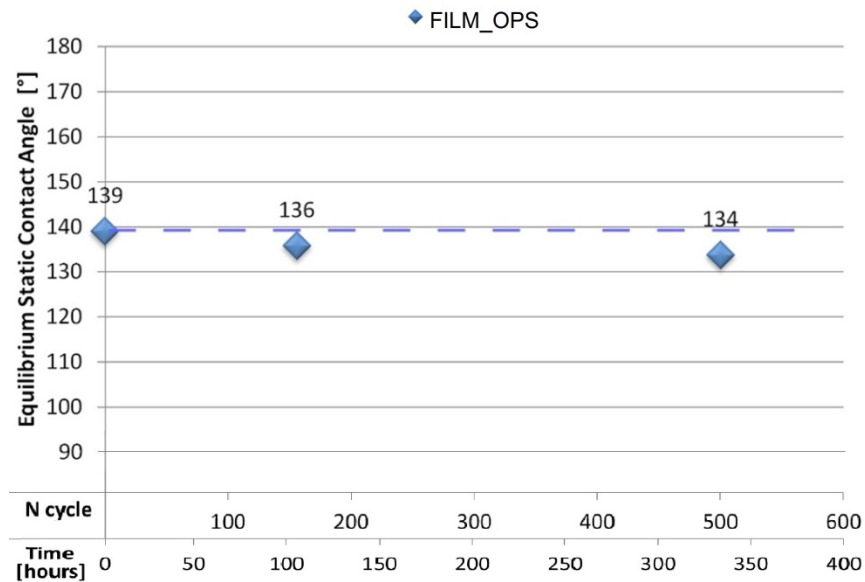
Figure 55: Measurement of the equilibrium contact angle on *FILM_OPS* after 0-156-506 thermal cycle

Chapter 7

7 Conclusions and perspectives

The effect of wettability on the pool boiling characteristics is investigated, carrying out experiments and simulations for boiling on different surfaces with varying given wettability characteristics.

The pool boiling phenomena is characterized by three important parameters: onset boiling temperature (T_{ONB}), the heat transfer coefficient (HTC) and the critical heat flux (CHT). A literature review shows that it is possible to improve these parameters by modifying the topology (at macro or even at micro/nano scale) and wettability of the surface (wettability of a surface can be can be characterized by equilibrium contact angle).

The conclusions of this work can be withdrawn as follow:

> ➢ The wettability influences the nucleation, the growth and detachment of the bubbles. The analysis of the experimental

results confirmed that the SHS requires a lower wall-superheat for the T_{ONB} to occur (as already shown in literature [42]). For our super-hydrophobic coating (Glaco Mirror Coat Zero©) it is observed a $T_{ONB}=102°C$, 12% less than uncoated sample ($T_{ONB}=117°C$ on stainless steel). Moreover, multiple nucleation sites are initially activated that coalesce to create a vapor film on the surface, if the super-hydrophobic coating covers all the surface.

➢ Using the same sample with a micro cavity in the center, in the case the inner wall of the micro cavity is super-hydrophobic (SHS_cavity) there is a reduction of the T_{ONB} (104°C) compared to the same sample with hydrophilic cavity (T_{ONB} 114°C). In this case the super-hydrophobicity influence only the nucleation of the single bubble (reducing the T_{ONB}). However the evolution of the bubble (growth and detachment) is the same for both case, because this takes place on the same surface (outside the cavity) with the same wettability.

➢ The super-hydrophobicity helps to sustain the boiling even with the present of a cross flow close to the wall. Two outcomes are observed: static bubble and pool boiling. The

ΔT_{onb} (when pool boiling regime appears) in this test is about 10-13°C.

Furthermore, one of the HPiS cases is also reproduced numerically using an enhanced VOF-based numerical model that is coupled with heat transfer and phase-change. This is done in order to further check the ability of the proposed numerical model to capture dynamic bubble growth characteristics, such as the time evolution of the apparent contact angles, bubble detachment time and the equivalent bubble detachment diameter. For this purpose two different numerical treatments for the triple-line contact angle are used (a static/constant contact angle and a dynamic contact angle treatment) and the results are compared with the corresponding experimental data, showing a good agreement.

Finally a new coating based on SH polymeric composition is proposed. The proposed coating is able to reduce the T_{ONB} as well as inhibit the formation of a vapor film on the interface solid-liquid. This is realized by the creation of a heterogeneous surface with SHS points (SHS grains formed by the SH polymeric solution OPS) dispersed on top of a hydrophilic surface (stainless steel surface). The proposed coating has an excellent thermal resistance. A thermal cycle test shows that there is no degradation of SH properties of the coating in pool boiling condition even after 506 thermal cycles. Therefore the SH polymeric composition can successfully use as coating in real heat transfer application. This direction

is rather new and can be further explored for applications other than those discussed in this thesis. Along with this pursuit, future research should need to develop the best procedure to apply the coating on a curvature geometry (e.g. in a tube or channel), as in many devise for heat transfer. Also improvement of the method for increase the mechanical resistance of the coating (briefly presented in chapter 6.2) should be investigated further.

List of Publication

[1] THERMOPEDIA, http://thermopedia.com/.

[2] Tabeling, P., Introduction to Microfluidics.

[3] Fabio Villa, M. M., Joël De Coninck, 2016, "Equilibrium Contact Angle at Boiling Condition," 27th Annual Conference on Liquid Atomization and Spray SystemsBrighton, UK.

[4] Jaikumar, A., and Kandlikar, S. G., 2015, "Enhanced pool boiling for electronics cooling using porous fin tops on open microchannels with FC-87," Applied Thermal Engineering, 91, pp. 426-433.

[5] Thome, J. R., 2004, "Boiling in microchannels: A review of experiment and theory," International Journal of Heat and Fluid Flow, 25(2), pp. 128-139.

[6] Baldassari, C., and Marengo, M., 2013, "Flow boiling in microchannels and microgravity," Progress in Energy and Combustion Science, 39(1), pp. 1-36.

[7] Steinke, M. E., and Kandlikar, S. G., 2004, "An experimental investigation of flow boiling characteristics of water in parallel microchannels," Journal of Heat Transfer, 126(4), pp. 518-526.

[8] Huh, D., Kuo, C. H., Grotberg, J. B., and Takayama, S., 2009, "Gas–liquid two-phase flow patterns in rectangular polymeric microchannels: effect of surface wetting properties," New journal of physics, 11, p. 75034.

[9] Nukiyama, S., 1934, "The Maximum and Minimum Values of Heat Q Transmitted From Metal to Boiling Water Under Atmospheric Pressure," Journal of Japanese Society of Mechanical Engineering, 37, pp. 367-374.

[10] Farber, E. A., Scorah, E.L., 1948, "Heat transfer to water boiling under pressure," Trans ASME, 70, pp. 369-384.

[11] Lavine, F. P. I. a. D. P. D. a. T. L. B. a. A. S., 2006, Fundamentals of Heat and Mass Transfer, John Wiley \& Sons.

[12] Bankoff, S. G., 1958, "Entrapment of gas in the spreading of a liquid over a rough surface," AIChE Journal, 4(1), pp. 24-26.

[13] Liu, D., Lee, P.-S., and Garimella, S. V., 2005, "Prediction of the onset of nucleate boiling in microchannel flow," International Journal of Heat and Mass Transfer, 48(25–26), pp. 5134-5149.

[14] Mieczyslaw E., J. R. T., 2008, Nucleate Boiling on Micro-Structured Surfaces.

[15] Yih-Yun Hsu, R. W. G., 1986, "Transport Processes in Boiling and Two-Phase Systems: Including Near-Critical Fluids," p. 589

[16] Basu, N., Warrier, G. R., and Dhir, V. K., 2002, "Onset of Nucleate Boiling and Active Nucleation Site Density During Subcooled Flow Boiling," Journal of Heat Transfer, 124(4), pp. 717-728.

[17] Hsu, Y. Y., 1962, "On the Size Range of Active Nucleation Cavities on a Heating Surface," Journal of Heat Transfer, 84(3), pp. 207-213.

[18] Kandlikar, S. G., 1999, Handbook of Phase Change: Boiling and Condensation.

[19] Rohsenow, W. M., and Massachusetts Institute of Technology. Division of Industrial, C., 1951, A Method of Correlating Heat Transfer Data for Surface Boiling of Liquids, M.I.T. Division of Industrial Cooporation.

[20] Zuber, N., 1959, Hydrodynamic aspects of boiling heat transfer (thesis), United States Atomic Energy Commission, Technical Information Service ; Clearinghouse for Federal Scientific and Technical Information, [Washington, D.C. : Springfield, Va.

[21] Lienhard, J. H., Dhir, V. K., Lewis Research, C., and University of, K., 1973, Extended hydrodynamic theory of the peak and minimum pool boiling heat fluxes, National Aeronautics and Space Administration ; For sale by the National Technical Information Service], Washington, D.C. : [Springfield, Va.

[22] Deng, D., Feng, J., Huang, Q., Tang, Y., and Lian, Y., 2016, "Pool boiling heat transfer of porous structures with reentrant cavities," International Journal of Heat and Mass Transfer, 99, pp. 556-568.

[23] Das, A. K., Das, P. K., and Saha, P., 2009, "Performance of different structured surfaces in nucleate pool boiling," Applied Thermal Engineering, 29(17–18), pp. 3643-3653.

[24] Webb, R. L., 1981, "The Evolution of Enhanced Surface Geometries for Nucleate Boiling," Heat Transfer Engineering, 2(3-4), pp. 46-69.

[25] Zhong, D., Meng, J. a., and Li, Z., 2016, "Experimental study of saturated pool boiling from downward facing structured surfaces," International Journal of Thermal Sciences, 108, pp. 52-61.

[26] Xu, P., Li, Q., and Xuan, Y., 2015, "Enhanced boiling heat transfer on composite porous surface," International Journal of Heat and Mass Transfer, 80, pp. 107-114.

[27] Kim, D. E., Yu, D. I., Jerng, D. W., Kim, M. H., and Ahn, H. S., 2015, "Review of boiling heat transfer enhancement on micro/nanostructured surfaces," Experimental Thermal and Fluid Science, 66, pp. 173-196.

[28] Kurihara, H. M., and Myers, J. E., 1960, "The effects of superheat and surface roughness on boiling coefficients," AIChE Journal, 6(1), pp. 83-91.

[29] Kang, M.-G., 2000, "Effect of surface roughness on pool boiling heat transfer," International Journal of Heat and Mass Transfer, 43(22), pp. 4073-4085.

[30] Jones, B. J., McHale, J. P., and Garimella, S. V., 2009, "The Influence of Surface Roughness on Nucleate Pool Boiling Heat Transfer," Journal of Heat Transfer, 131(12), pp. 121009-121009.

[31] Kim, S. H., Lee, G. C., Kang, J. Y., Moriyama, K., Kim, M. H., and Park, H. S., 2015, "Boiling heat transfer and critical heat flux evaluation of the pool boiling on micro structured surface," International Journal of Heat and Mass Transfer, 91, pp. 1140-1147.

[32] Lu, L., Fu, T., Tang, Y., Tang, T., Tang, B., and Wan, Z., 2016, "A novel in-situ nanostructure forming route and its application in pool-boiling enhancement," Experimental Thermal and Fluid Science, 72, pp. 140-148.

[33] Young Lee, C., Hossain Bhuiya, M. M., and Kim, K. J., 2010, "Pool boiling heat transfer with nano-porous surface," International Journal of Heat and Mass Transfer, 53(19–20), pp. 4274-4279.

[34] Bourdon, B., Rioboo, R., Marengo, M., Gosselin, E., and De Coninck, J., 2012, "Influence of the wettability on the boiling onset," Langmuir, 28(2), pp. 1618-1624.

[35] Dhir, V. K., 1991, "Nucleate and transition boiling heat transfer under pool and external flow conditions," International Journal of Heat and Fluid Flow, 12(4), pp. 290-314.

[36] Adam, N. K., 1964, "The Chemical Structure of Solid Surfaces as Deduced from Contact Angles," Contact Angle, Wettability, and Adhesion, AMERICAN CHEMICAL SOCIETY, pp. 52-56.

[37] Wenzel, R. N., 1936, "Resistance of Solid Surfaces to Wetting by Water," Industrial & Engineering Chemistry, 28(8), pp. 988-994.

[38] Cassie, A. B. D., and Baxter, S., 1944, "Wettability of porous surfaces," Transactions of the Faraday Society, 40(0), pp. 546-551.

[39] Fowkes, F. M., 1964, Contact Angle, Wettability, and Adhesion, AMERICAN CHEMICAL SOCIETY.

[40] Fan, L.-W., Li, J.-Q., Li, D.-Y., Zhang, L., and Yu, Z.-T., 2014, "Regulated transient pool boiling of water during quenching on nanostructured surfaces with modified wettability from superhydrophilic to superhydrophobic," International Journal of Heat and Mass Transfer, 76, pp. 81-89.

[41] Bourdon, B., Bertrand, E., Di Marco, P., Marengo, M., Rioboo, R., and De Coninck, J., 2015, "Wettability influence on the onset temperature of pool boiling: Experimental evidence onto ultra-smooth surfaces," Advances in Colloid and Interface Science, 221, pp. 34-40.

[42] Malavasi, I., Bourdon, B., Di Marco, P., de Coninck, J., and Marengo, M., 2015, "Appearance of a low superheat "quasi-Leidenfrost" regime for boiling on superhydrophobic surfaces," International Communications in Heat and Mass Transfer, 63, pp. 1-7.

[43] Takata, Y., Hidaka, S., and Kohno, M., 2012, "Effect of Surface Wettability on Pool Boiling: Enhancement by Hydrophobic Coating," International Journal of Air-Conditioning and Refrigeration, 20(01), p. 1150003.

[44] Wang, C. H., and Dhir, V. K., 1993, "Effect of Surface Wettability on Active Nucleation Site Density During Pool Boiling of Water on a Vertical Surface," Journal of Heat Transfer, 115(3), pp. 659-669.

[45] Jo, H., Ahn, H. S., Kang, S., and Kim, M. H., 2011, "A study of nucleate boiling heat transfer on hydrophilic, hydrophobic and heterogeneous wetting surfaces," International Journal of Heat and Mass Transfer, 54(25), pp. 5643-5652.

[46] Takata, Y., Hidaka, S., and Uraguchi, T., 2006, "Boiling Feature on a Super Water-Repellent Surface," Heat Transfer Engineering, 27(8), pp. 25-30.

[47] Betz, A. R., Jenkins, J., Kim, C.-J. C., and Attinger, D., 2013, "Boiling heat transfer on superhydrophilic, superhydrophobic, and superbiphilic surfaces," International Journal of Heat and Mass Transfer, 57(2), pp. 733-741.

[48] Aydar, A. Y., Rodriguez-Martinez, V., and Farkas, B. E., 2016, "Determination and modeling of contact angle of Canola oil and olive oil on a PTFE surface at elevated temperatures using air or steam as surrounding media," LWT - Food Science and Technology, 65, pp. 304-310.

[49] Good, R. J., and Girifalco, L. A., 1960, "A Theory for Estimation of Surface and Interfacial Energies. Iii. Estimation of Surface Energies of Solids From Contact Angle Data," The Journal of Physical Chemistry, 64(5), pp. 561-565.

[50] Petke, F. D., and Ray, B. R., 1969, "Papers Presented at the 43rd National Colloid SymposiumTemperature dependence of contact angles of liquids on polymeric solids," Journal of Colloid and Interface Science, 31(2), pp. 216-227.

[51] Osborne III, and L, K., 2009, "Temperature-Dependence of the Contact Angle of Water on Graphite, Silicon, and Gold," master, Worcester Polytechnic Institute.

[52] Kandlikar, S. G., and Steinke, M. E., 2002, "Contact angles and interface behavior during rapid evaporation of liquid on a heated surface," International Journal of Heat and Mass Transfer, 45(18), pp. 3771-3780.

[53] Terpiowski, K., 2015, "Influence of the ambient temperature on water and diiodomethane contact angle with quartz surface," Annales Chemia, 70(1).

[54] Stock, P., Utzig, T., and Valtiner, M., 2015, "Direct and quantitative AFM measurements of the concentration and temperature dependence of the hydrophobic force law at nanoscopic contacts," Journal of Colloid and Interface Science, 446, pp. 244-251.

[55] Fabio Villa*, M. M., Joël De Coninck, 2016, "Equilibrium Contact Angle at Boiling Condition " ILASS – Europe 2016, 27th Annual Conference on Liquid Atomization and Spray SystemsBrighton, UK.

[56] Weisensee, P. B., Neelakantan, N. K., Suslick, K. S., Jacobi, A. M., and King, W. P., 2015, "Impact of air and water vapor environments on the hydrophobicity of surfaces," Journal of Colloid and Interface Science, 453, pp. 177-185.

[57] Anastasios Georgoulas, M. A. a. M. M., 2017, "An enhanced VOF method coupled with heat transfer and phase change to characterise bubble detachment in saturated pool boiling," Submitted to "Energies", .

[58] Prabhudharwadkar, D., Lopez-de-Bertodano, M. A., Hibiki, T., and Buchanan Jr, J. R., 2014, "Assessment of subcooled boiling wall boundary correlations for two-fluid model CFD," International Journal of Heat and Mass Transfer, 79, pp. 602-617.

[59] Cheung, S. C. P., Vahaji, S., Yeoh, G. H., and Tu, J. Y., 2014, "Modeling subcooled flow boiling in vertical channels at low pressures – Part 1: Assessment of empirical correlations," International Journal of Heat and Mass Transfer, 75, pp. 736-753.

[60] Harlow, F. H., and Welch, J. E., 1965, "Numerical Calculation of Time-Dependent Viscous Incompressible Flow of Fluid with Free Surface," Physics of Fluids, 8(12), pp. 2182-2189.

[61] Tryggvason, G., Bunner, B., Esmaeeli, A., Juric, D., Al-Rawahi, N., Tauber, W., Han, J., Nas, S., and Jan, Y.-J., 2001, "A front-tracking method for the computations of multiphase flow," J. Comput. Phys., 169(2), pp. 708-759.

[62] Hirt, C. W., Amsden, A. A., and Cook, J. L., 1974, "An arbitrary Lagrangian-Eulerian computing method for all flow speeds," Journal of Computational Physics, 14(3), pp. 227-253.

[63] Hirt, C. W., and Nichols, B. D., 1981, "Volume of fluid (VOF) method for the dynamics of free boundaries," Journal of Computational Physics, 39(1), pp. 201-225.

[64] Osher, S., and Sethian, J. A., 1988, "Fronts propagating with curvature-dependent speed: Algorithms based on Hamilton-Jacobi formulations," Journal of Computational Physics, 79(1), pp. 12-49.

[65] Brackbill, J. U., Kothe, D. B., and Zemach, C., 1992, "A continuum method for modeling surface tension," J. Comput. Phys. %@ 0021-9991, 100(2), pp. 335-354.

[66] Hardt, S., and Wondra, F., 2008, "Evaporation model for interfacial flows based on a continuum-field representation of the source terms," Journal of Computational Physics, 227(11), pp. 5871-5895.

[67] Georgoulas, A., Koukouvinis, P., Gavaises, M., and Marengo, M., 2015, "Numerical investigation of quasi-static bubble growth and detachment from submerged orifices in isothermal liquid pools: The effect of varying fluid properties and gravity levels," International Journal of Multiphase Flow, 74, pp. 59-78.

[68] A. Georgoulas, M. M., "Numerical Investigation of Adiabatic Growth and Detachment of Gas/vapor Bubbles Injected From a Submerged Orifice at Various Surface Inclinations," Proc. 15th International Heat Transfer Conference.

[69] Georgoulas, A., and Marengo, M., "Numerical simulation of pool boiling: the effects of initial thermal boundary layer, contact angle and wall superheat," Proc. UK Heat Transfer Conference.

[70] Georgoulas, A., and Marengo, M., "Numerical simulation of flow boiling in micro-channels: bubble growth, detachment and coalescence," Proc. UK Heat Transfer Conference.

[71] Hoang, D. A., van Steijn, V., Portela, L. M., Kreutzer, M. T., and Kleijn, C. R., 2013, "Benchmark numerical simulations of segmented two-phase flows in microchannels using the Volume of Fluid method," Computers & Fluids, 86, pp. 28-36.

[72] Suraj, S. D., Lakshman, A., and Mario, F. T., 2012, "Evaluating the performance of the two-phase flow solver interFoam," Computational Science & Discovery, 5(1), p. 014016.

[73] Schrage, R. W., 1953, "A theoretical study of interphase mass transfer," Columbia University Press, New York.

[74] Kunkelmann, C., and Stephan, P., 2009, "CFD Simulation of Boiling Flows Using the Volume-of-Fluid Method within OpenFOAM," Numerical Heat Transfer, Part A: Applications, 56(8), pp. 631-646.

[75] Fabio Villa, A. G., Marco Marengo, Paolo Di Marco, Joël De Coninck "Pool boiling versus surface wettability characteristics," Proc. World Congress on Momentum, Heat and Mass Transfer (MHMT'16).

[76] Situ, R., Ishii, M., Hibiki, T., Tu, J. Y., Yeoh, G. H., and Mori, M., 2008, "Bubble departure frequency in forced convective subcooled boiling flow," International Journal of Heat and Mass Transfer, 51(25–26), pp. 6268-6282.

[77] Podowski, R., Drew, D., Lahey Jr, R., and Podowski, M., "A mechanistic model of the ebullition cycle in forced convection subcooled boiling," Proc. Eighth international topical meeting on nuclear reactor thermal-hydraulics.

[78] Chi-Yeh, H., and Griffith, P., 1965, "The mechanism of heat transfer in nucleate pool boiling—Part I," International Journal of Heat and Mass Transfer, 8(6), pp. 887-904.

[79] Hamzekhani, S., Maniavi Falahieh, M., and Akbari, A., 2014, "Bubble departure diameter in nucleate pool boiling at saturation: Pure liquids and binary mixtures," International Journal of Refrigeration, 46, pp. 50-58.

[80] Rainey, K. N., You, S. M., and Lee, S., 2003, "Effect of pressure, subcooling, and dissolved gas on pool boiling heat transfer from microporous, square pin-finned surfaces in FC-72," International Journal of Heat and Mass Transfer, 46(1), pp. 23-35.